Prediction and Minimization of Excessive Distortions and Residual Stresses
in Compliant Assembled Structures

by

Anderson Yoshizato

B.Eng, University of São Paulo - Brazil, 1999

A Thesis Submitted in Partial Fulfillment
of the Requirements for the Degree of

MASTER OF APPLIED SCIENCE

in the Department of Mechanical Engineering

Supervisory Committee

Prediction and Minimization of Excessive Distortions and Residual Stresses
in Compliant Assembled Structures

by

Anderson Yoshizato
B.Eng, University of São Paulo - Brazil, 1999

Supervisory Committee

Dr. Curran Crawford (Department of Mechanical Engineering)
Supervisor

Dr. Keivan Ahmadi (Department of Mechanical Engineering)
Departmental Member

Abstract

Supervisory Committee

Dr. Curran Crawford (Department of Mechanical Engineering)
Supervisor

Dr. Keivan Ahmadi (Department of Mechanical Engineering)
Departmental Member

The procedure of joining flexible or nonrigid parts using applied loads is called compliant assembly, and it is widely used in automotive, aerospace, electronics, and appliance manufacturing. Uncontrolled assembly processes may produce geometric errors that can exceed design tolerances and induce an increment of elastic energy in the structure due to the accumulation of internal stresses. This condition might create unexpected deformations and residual stress distributions across the structure that compromise product functionality. This thesis presents a method based on nonlinear Finite Element Analysis (FEA), metamodelling, and optimization techniques to provide accurate and on-time shimming strategies to support the definition of optimum assembly strategies. An example of the method on a typical aerospace wing box structure is demonstrated in the present study. The delivered outputs intend to support the production line by anticipating the response of the structure under a specific assembly condition and presenting alternative assembly strategies that can be applied to address eventual predicted issues on product requirements.

Table of Contents

List of Tables

List of Figures

Nomenclature

CAD	Computerized Assisted Design
CAE	Computerized Assisted Engineering
CMM	Computerized Measurement Machine
DOE	Design of Experiments
DOF	Degrees of Freedom
FEA	Finite Element Analysis
FEM	Finite Element Method
FE	Finite Element
GA	Genetic Algorithm
MCS	Monte Carlo Simulation
MIC	Method of Influence Coefficients
MOGA	Multi-Objective Genetic Algorithm
MRB	Materials Review Board
MRR	Maximum Relative Residual
NSGA-II	Non-dominated Sorted Genetic Algorithm-II
OSF	Optimal Space-Filling
PCA	Principal Component Analysis
PRESS$_{RMSE}$	Predicted residual error sum of squares
RAAE	Relative Average Absolute Error
RMAE	Relative Maximum Absolute Error
RMSE	Root Mean Squared Error
RRMSE	Relative Root Mean Squared Error
RSM	Response Surface Methodology

Symbols

$[K_u]$	Stiffness matrix of the set of parts positioned on the assembly fixture
$[K_w]$	Stiffness matrix of the fastened structure
$[S_{wu}]$	Sensitivity matrix
$\{F_u\}$	Clamping Forces vector
$\{F_w\}$	Spring Back Reaction vector
$\{U_w\}$	Structure Spring Back vector
$\{V_u\}$	Vector nominal positions at the clamp locations
$\{V_u\}$	Part Deviations vector

Acknowledgments

I would like to express my gratitude to my supervisor, Dr. Curran Crawford, who has supported me in the development of this project and provided me with a unique learning opportunity at the University of Victoria.

Dedication

This report is dedicated to my partner Emi and my daughters Miyuki and Naomi, who have been my main source of motivation to overcome all challenges in life.

1 - Introduction

Mechanical structures aim to carry loads from where they are applied to where the structures are supported most efficiently. Efficiency in this context means to perform the designed function with the least use of material. Aside from the benefits of the product performance, lightweight components may affect the operational costs by reducing the required raw material, processing time, handling and transportation expenses. As a result, geometries become thinner and slenderer, and structures present either a box beam or a truss design configuration, preferably.

Dimensional integrity is an essential aspect of product quality in many manufactured consumer goods. Dimensional issues may adversely affect the final product functionality and process performance. Variability in the quality of raw material, production capabilities and working conditions can potentially cause geometric variations in the produced components. Uncontrolled assembly processes may also produce geometric errors that can exceed the design tolerances of the structure [1].

The relationship between residual stresses and mechanical properties has been an essential topic in the design of lighter and more efficient components, as structural failures can be caused by the combination of residual and applied stresses. According to Withers et al. [2], micro residual stresses are generated from misfits in the natural shape between different regions, different parts, or different phases. Whereas, macro residual stresses in engineering components are derived from the interaction between misfitting parts within an assembly. For simplification, the term residual stress refers to macro residual stress in this report. Thus, the compliant forces required to mate non-ideal parts on the jig or another

component induce an increment of elastic energy in the structure as a consequence of the accumulation of internal stresses. When the assembled structure is released from the fixture and springs back, the elastic energy and stress distribution are altered, creating a new condition of equilibrium. However, this condition might develop unexpected deformations and residual stresses distributions across the structure that compromise product functionality [2].

Slender parts, such as the aeronautical components illustrated in Figure 1, are more likely to be affected by distortions caused by micro residual stresses. The geometrical sensitivity of slender parts is a consequence of their lower deformation resistance to accommodate the redistribution of internal stresses reaching a new equilibrium condition. Consequently, non-rigid parts are usually designed with a broader tolerance range as their variation can be managed by forcing the contact of mating surfaces under the yield and stress limits.
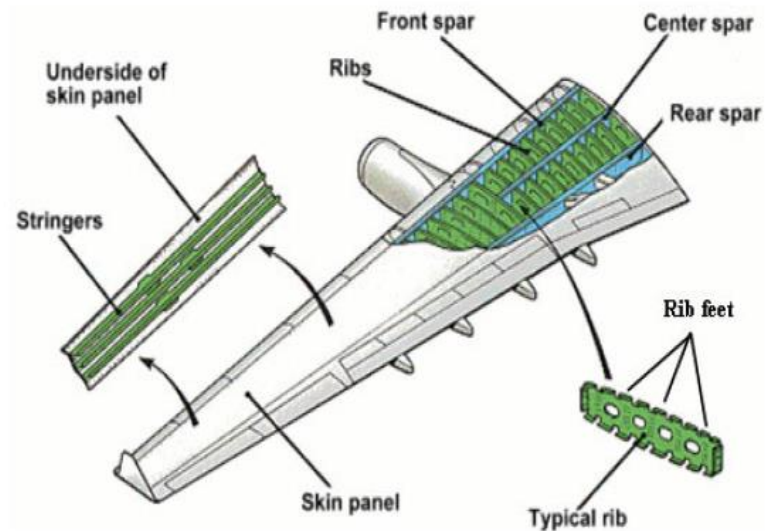
Figure 1 – Wing Box Assembly - Extracted from [1]

The procedure of joining flexible or nonrigid parts using applied loads is called compliant assembly process, and it is widely used in automotive, aerospace, electronics, and appliance manufacturing [2, 3]. As a reference, Figure 2 shows the Bombardier Global 5000/6000 wing box assembly jig locate at Mitsubishi Heavy Industries (MHI) facility.
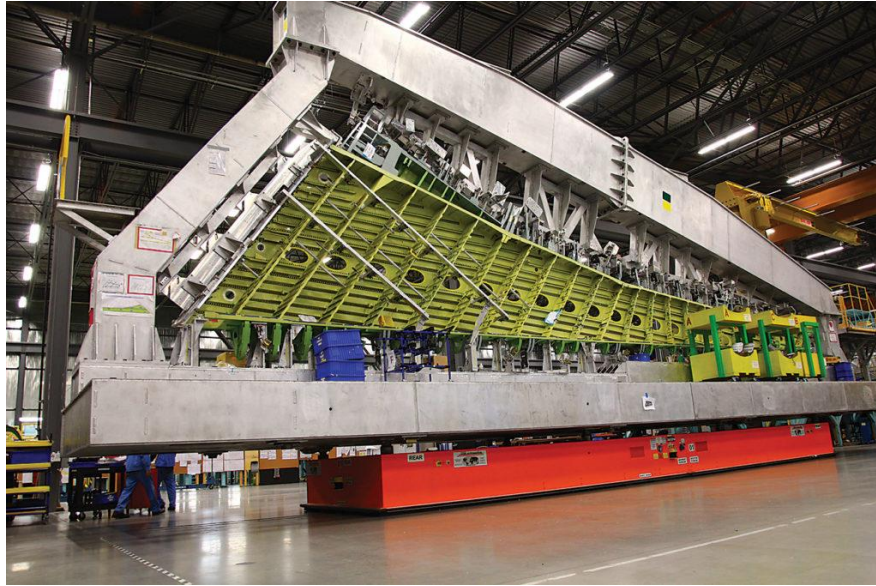
Figure 2 - Global 5000/6000 assembly jig at MHI – Extracted from [4]

The susceptibility to distortions caused by compliant forces increases the chances of aerostructures to present excessive dimensional variations and unbalanced residual stress distributions. Cantilever structures, such as aircraft wings and stabilizers, are examples of slender products with strict dimensional requirements and highly prone to distortions.

Real-world large aerostructures, such as wing boxes, might experience deviations that demand flight control surfaces adjustments (trimming) to balance the aircraft moments. Besides the costs associated with the measurement and adjustments, the corrective action might degrade the aircraft performance due to the increased trim drag necessary to balance the flight behaviour. Furthermore, because of measurement difficulties, the effects of the

residual stresses, induced during the assembly process, are not considered for fatigue life computing.

Most of the literature focuses on preventing geometrical and cumulative stress problems through the determination of optimum tolerance allocation. Solutions based on these approaches are implemented in the design stage and hence tend to be more robust and cheaper. However, dimensional issues commonly arise in the production line as well, and in-process actions must be taken to mitigate their impacts on the final product. The importance of in-process approaches in aerospace assembly is due to the difficulties and high costs to produce large and complex structural components within a strict tolerance range. Also, the long processing lead time to replace a non-conform component pushes a technical solution that avoids the financial and planning drawbacks of scrapping the non-conform component, e.g. through changes in the assembly process or parts reworks. Consequently, approved as-produced parts with minor geometrical issues may be used in the assembly line under the material review board (MRB) approval. Such not-planned conditions may require additional compliant forces that would increase the likelihood of unexpected deformations in the final structure. Thus, for either design or in-process improvement purposes, it is essential to determine how the variations propagate and influence the overall geometry of the structure with the as-produced parts. Furthermore, for fatigue strength assessment, it is necessary to understand how the compliant forces affect the residual stresses distribution and the fatigue performance consequently. In addition, a proper comprehension of the assembled structure behaviour under compliant loadings provides essential information to develop more robust designs and to manage issues with non-ideal parts in the assembly line.

1.1. Contributions

The present methodology aims to determine an optimum in-process assembly strategy, based on as-produced parts, to minimize potential issues caused by excessive distortions and residual stresses in compliant assemblies. Since the method is designed to be applied on the assembly line, its accuracy and response time are critical factors for its implementation. Therefore, modelling techniques that potentially increase the speed of the analysis while maintaining satisfactory outputs accuracy need to be assessed and implemented.

Compliant forces used in the assembly process affect the stress distribution. As a consequence, they influence the overall distortions and residual stresses of the structure. The remaining gaps are the result of the compliant force intensities used to mate the distorted components. Since gaps and complying forces are negatively correlated, the higher the compliant loading, the smaller the gap left in between mating surfaces. Additionally, in case the remaining gap exceeds the design tolerance or stress analysis, a shim or similar filler is used to assure a tolerance fit between the parts and prevent unexpected stresses in the structure, as illustrated in Figure 3.
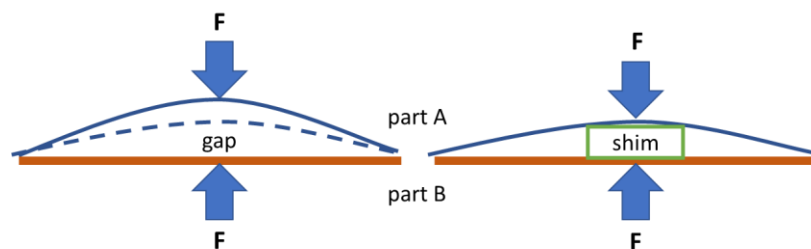
Figure 3 - Gaps caused by Compliant Forces and Shimming

In aeronautical assembled structures, solid (flat and tapered) and laminated metallic shims, as presented in Figure 4, are the most common solutions to fill eventual gaps in between mating surfaces. In some non-structural applications, liquid shims are also an alternative.

Figure 4 – Laminated Shims – Extracted from Assembly Magazine [5]

Compliant forces have an effect over the geometrical variation of slender assemblies. Also, there exists a direct relationship between the left gaps and the stress distribution across the structure. As a consequence, it is reasonable to consider shimming as a mechanism to manage compliant loadings to manage the residual stress distribution and displacements along with the structure. Thus, this work presents a methodology to determine an optimized shimming distribution strategy that can mitigate excessive distortions and residual stresses caused by non-ideal as-produced parts. This thesis presents a method based on nonlinear Finite Element Analysis (FEA), metamodelling, and optimization techniques to provide accurate and on-time shimming strategies to support the definition of optimum assembly strategies. An example of the method on a typical

aerospace wing box structure is demonstrated in the present study. The delivered outputs intend to support the production line by anticipating the response of the structure under a specific assembly condition and presenting alternative assembly strategies that can be applied to address eventual predicted issues on product requirements.

1.2.   Thesis Outline

This thesis is divided into six chapters. In chapter 1, the problem and challenges are contextualized, and the proposed solution is introduced. Chapter 2 presents the literature review of linear and nonlinear predictive models and methods to minimize problems with distortions and residual stresses in compliant assemblies. The modelling, metamodelling and optimization theories that support the proposed methodology are detailed in Chapter 3. In Chapter 4, a case study is set to demonstrate the feasibility of the method. The data, setup, steps and analysis criteria used in the case study are detailed. The computed results of the case study are presented in Chapter 5, and finally, the conclusion over the results of the case study and the methodology, as well as suggestions of future developments, are outlined in Chapter 6.

2 -   Literature Review

Before the introduction of numerical simulation methods, the variation of compliant assemblies was performed considering components as rigid bodies. In this approach, the individual deviations are stacked-up assuming a rigid body behaviour in order to determine the overall variation of the compliant assembled structure. As a result, this solution imposes a conservative tolerance allocation in the product, since the effects of the compliant forces and deformations are not considered in the analysis. Furthermore, the prediction of distortions and residual stresses on complex structures is not possible without considering the capabilities of numerical simulation methods. Therefore, computational methods are fundamental to understand the mechanisms of interaction among flexible parts and to establish a proper correlation between components and assembly deviations.

2.1.   Linear Analysis Approach

Despite the higher accuracy of nonlinear Finite Element Method (FEM), its application in Monte Carlo Simulation (MCS) and optimization analysis of complex models is limited because of the computational demand and high processing time. Thus, the fast response and relatively more straightforward implementation of linear FE models have justified their extensive use of statistical-based simulation analysis. In 1997, Liu and Hu [3] proposed a method to calculate variations in deformable sheet metal assemblies based on the deformations found in incoming parts and tooling. By breaking down the assembly process into four steps, as depicted in Figure 5, the relationship between the deviations of incoming parts and the resultant spring back of the assembly is determined.
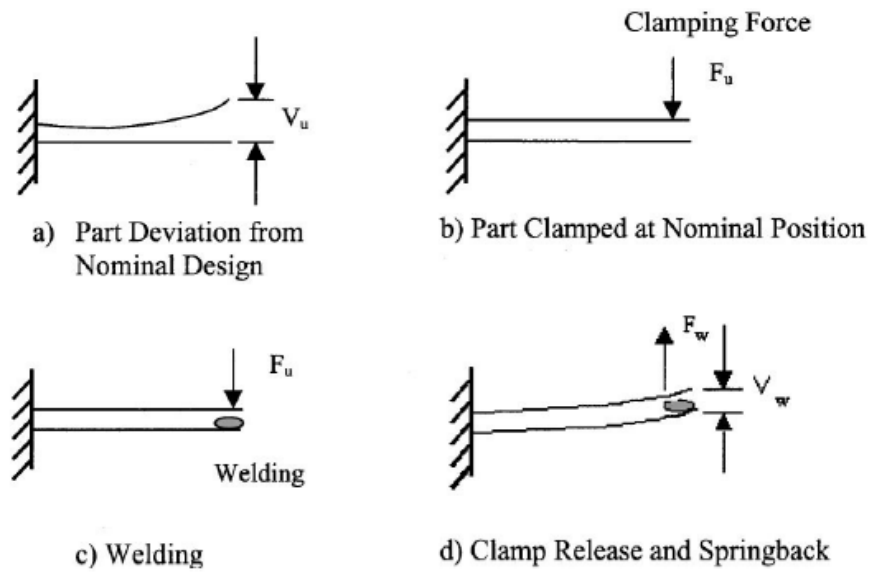
Figure 5 - Four-step compliant assembly process - Extracted from [6]

The clamping forces $\{F_u\}$ required to bring the deflected edge to the nominal position can be calculated according to Equation 1:

$$\{F_u\} = [K_u]\{V_u\} \tag{1}$$

where $\{V_u\}$ is defined as the parts deviation vector measured relative to the nominal positions at the clamp locations and $[K_u]$ defined as the stiffness matrix of the set of parts positioned on the assembly fixture. The resulting forces vector $\{F_w\}$ is the reaction created by the spring back of the assembly after the clamping forces are removed. With $[K_w]$ representing the stiffness matrix of the fastened structure, the relationship between the spring back vector of the entire structure $\{U_w\}$ and the reaction forces vector $\{F_w\}$ is presented in Equation 2:

$$[K_w]\{U_w\} = \{F_w\}, \text{ or } \{U_w\} = [K_w]^{-1}\{F_w\} \tag{2}$$

Considering the clamping and reaction forces vectors identical (Equation 3), the relationship between the deviation of the part vector $\{V_u\}$ and the spring back vector $\{U_w\}$ can be reorganized as described in Equation 4.

$$\{F_w\} = \{F_u\} \tag{3}$$

$$\{U_w\} = [K_w]^{-1}[K_u]\{V_u\} \tag{4}$$

$[K_w]^{-1}[K_u]$ presented in Equation 4 is also known as Sensitivity Matrix $[S_{wu}]$, which indicates how sensitive the assembly deviation vector $\{U_w\}$ is to the part deviations vector $\{V_u\}$ as described in the Mechanist Variation Model (Equation 5).

$$\{U_w\} = [S_{wu}]\{V_u\} \tag{5}$$

The mechanist variation model is derived from the inverse of the stiffness matrix of the assembled structure. At the time of Liu and Hu's [2] publication, most FEA solvers did not provide user access to the stiffness matrix, and the memory capacity had restrictions to manipulate a large amount of data. As a consequence, they proposed the method of influence coefficients (MIC) to derive the Sensitivity matrix $[S_{wu}]$ based on only two FEM runs, hence overcoming the computational limitations. Although the mechanist variation model and MIC enabled more realistic analysis of compliant assemblies in comparison to the rigid-body stack up approach, some simplifications inherent to the linear method, such as the neglection of geometrical changes in large displacements and contact reactions, have affected the accuracy of the outputs. Because of such constraints in the analysis, Camelio

et al. [7] reviewed the assumption of an independent source of variations by taking into consideration the geometric covariance of the neighbouring points on the same surface.

2.2.   Nonlinear Analysis Approach

Even though there were improvements in the accuracy of the outputs of linear FEA models, compliant assemblies are highly nonlinear complex processes, and the impacts of modelling simplifications on the outputs must be thoroughly evaluated.

Large nonlinear models with thousands of degrees of freedom (DOF) are computationally expensive and time-consuming. In fact, the improvement in output precision requires a smaller convergence criterion in the Newton-Raphson method, increasing the number of required iterations to reach convergence and hence higher processing time. The lack of efficient nonlinear modelling tools had limited the analysis for simplified linear models in the early studies of compliant assembly processes. As a result, forces and imperfections of the parts were not transferred via the contact surfaces. In addition, by omitting the contact mechanisms, the parts could penetrate each other, causing inaccuracies on the spring back and stresses calculation [8]. To prevent penetrations, Dahlstrom et al. [8] implemented a contact modelling technique to MIC. The model used a contact detection and a contact equilibrium search algorithm based on projections of nodes onto the elements. The contact detection was performed based on the projection, position and distance of slave nodes and master elements. The contact equilibrium was determined by forcing the penetrated slave nodes out of contact. However, changes in the stiffness matrix were neglected when parts were subjected and positioned, compromising the accuracy of the methodology. Ungemach et al. [9] proposed a retroactive method capable of addressing the penetration issues during clamping and spring back

calculation. Instead of following the entire procedure considering all individual contact cases, the computation is performed based on the classic MIC spring back analysis, and then the contact calculation is undertaken retroactively. Once the penetrations were identified, a method called direct elimination could be used to establish a linear system to correct the resulting spring back. Although a good approximation could be reached, the procedure had limitations for significant variations and penetrations. Furthermore, the dissolution of all penetrations may lead to the occurrence of tensile forces between the nodes compromising the accuracy of the results. Though the fast responses of the linear approach have enabled statistical simulations and optimization procedures, the inherent simplifications in the models compromise the quality of the results, limiting their use in more precise analysis.

A nonlinear model considering contact interactions was implemented by Xie et al. [10]. The method examined the six steps in the assembly process to determine components and tooling variation propagation in compliant assemblies. Thus, the methodology took part-part and part-tool contacts into consideration that improved the accuracy of the results derived from the analysis. As presented in Xie et al. [10], the convergence of models with contact elements is an important issue. Thus, several measures were considered to prevent penetrations and increase the stability of the model. The scheme to predict distortions and residual stresses of non-ideal parts based on nonlinear FE simulation is detailed in the workflow of Figure 6. Liao and Wang [11] conducted a nonlinear analysis considering friction in the contact. In the experiment, the friction factor value was changed to analyze the influence of their forces on the response of the assembly. The results showed that the friction factor has a minor impact on the measured displacements for the cases studied.

Furthermore, according to the experiments, it was observed that the nonlinear contact modelling could represent the assembly variation with high accuracy.
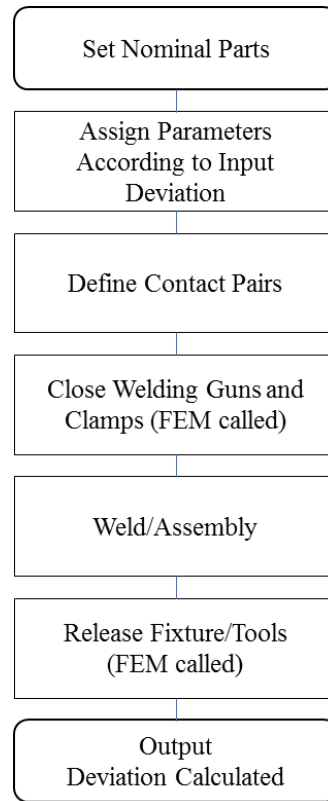
Figure 6 - Predictive contact assembly - Adapted from Xie et al. [5]

Although there are clear benefits of nonlinear FEA to represent the compliant assembly process, the analysis requires a complete simulation to determine the final spring back for each set of input deviations. Despite the numerous advances of FE solvers and hardware that have contributed to improving the feasibility of the analysis of computational demanding engineering problems, optimization and statistical analysis of large and complex nonlinear models are still prohibitive for timely restricted applications. Thus, though the nonlinear FE models provide more accurate outputs in comparison to the linear

approach, the processing time per iteration is still a critical issue that requires a complementary approach to overcome such limitations.

2.3. Distortion and Residual Stresses Management

Dimensional integrity is an essential aspect of product quality in many manufactured consumer goods. Out-of-specification distortions may adversely affect the final product functionality and process performance. In body-in-white structures, for instance, dimensional deviations might cause aesthetic issues due to the excessive gaps and steps. In aerospace structures, distortions exceeding the design tolerance might create unexpected drag forces in aerodynamic surfaces and functional problems in mechanisms. Furthermore, the fatigue strength can be compromised by the combination of tensile stresses of the loadings and the remaining residual stresses in the structure [12].

Since variations are present in all manufacturing variables and produced components, the assembly process should be robust enough to absorb some geometric deviations from the parts, while keeping the overall distortion and residual stresses under limits that would not affect the functionality of the structure. The minimization of the effects of misfitting components has been addressed by robust design and in-process approaches. The strategies adopted in the design stages rely on the tolerance allocation analysis of the components and assembly jigs in order to keep the product under the allowed design variations and production costs. Whereas, the in-process approach determines the optimum assembly strategy to deal with the non-ideal as-produced parts already available in the production line.

Most researches have focused on the development of tolerance allocation methods. An optimized tolerance distribution across parts and fixtures has a relevant impact on the

product performance and production costs, and hence it must be the first approach to constrain excessive distortion and residual stress.

Liu and Hu [3] coupled FEA and MCS using MIC to analyze the relationship between part deviations and assembly spring-back, which supported the definition of tolerance distribution across the assembled structure. Li et al. [13] proposed a method for tolerance allocation in multi-station compliant assemblies. The method is based on a hierarchical multilevel process and optimization strategy to determine tolerance specifications for incoming parts, subassemblies and station fixtures considering quality and cost targets. Yue et al. [14] worked on creating a set of product-oriented sensitivity indices to evaluate the robustness of multi-station compliant assemblies. Those indices would be used to estimate the sensitivities with no information about the incoming parts and tools variation, which is especially valuable in the design phases of a product. Dong and Kang [15] proposed the use of Response Surface Methodology (RSM) to represent an FEA model and overcome the excessive time-consuming in MCS to compute the deformation and residual stresses distribution of an assembly.

Although tolerance allocation analysis is meant to keep the variations within the design specifications, unavoidable and unexpected deviations in the fabrication process of the components can occur and cause significant product variability. For changes caused by unexpected distortions, mating issues can arise across the assembled structure and must be addressed to prevent error propagation and other critical quality issues. Thus, the in-process improvement approach, which considers as-produced parts and fixtures data, is a crucial tool to determine strategies that can mitigate the negative impacts of the unexpected variations in the assembly line. Although few works on the in-process assembly

improvement approach have been published, as most of the studies focus on tolerance allocation analysis, the topic has significant importance for aeronautical structures because of the high cost and the difficulties of dealing with strict requirements and distortions of large and slender structural components.

In another study, Hu and Camelio [16] presented a procedure that coupled variation simulation models with adaptative control tools to minimize assembly deviations based on the determination and application of fixture corrections. Wang and Ding [17] proposed a method to identify the primary sources of variations for a horizontal stabilizer using FEA and Principal Component Analysis (PCA). The pre-determined information, derived from the analysis, was coupled with real-world data by the Least Square fitting method allowing a more precise control during horizontal stabilizer assembly. Wang H. [18] developed a highly efficient method based on hybrid metamodels, derived from FEA simulation results and particle swarm optimization algorithm, to support the selection of as-produced components to be assembled.

Gaps are considered as the consequence of the assembly strategy to join components with non-ideal geometries. When the allowed compliant force is not enough to make the mating surfaces to match, gaps are left and are typically filled with shims. The stresses induced by the compliant forces have an impact on the geometric and stresses distribution along with the structure. When the assembled structure is released from the assembly jig or fixture, it might spring back, reaching a new configuration. Therefore, proper management of the compliant forces or gaps can potentially be used to mitigate issues with distortions and excessive residual stresses in assembled structures.

3 -   Methodology

This chapter presents an overview of the proposed methodology and the basic theory of each analysis step that support their application in compliant assembly problems. The present study focuses on the development of an in-process methodology to predict distortions and residual stresses in compliant assembled structures, composed of as-produced parts, and mitigate their impacts on product characteristics and performance. The methodology is divided into the following four main steps:

1. Physical modelling

2. Dimension reduction

3. Statistical modelling

4. Optimal solution search

Figure 7 describes the similarities and differences between the conventional and the proposed methods. It also presents the analysis time that the proposed methodology needs to accomplish in order to not impact the conventional production schedule.

In the conventional process, the critical dimensions of the parts are inspected for quality purposes, e.g. by a Computerized Measurement Machine (CMM), then the components are pre-assembled on the assembly jig, and the remaining gaps are measured for shims fabrication. During the pre-assembly operation, the parts are positioned and subjected to the mating surfaces and fastened temporarily. The remaining gaps are measured, and the data is forwarded for shims fabrication. Shims are then placed at the correspondent gap location, and the parts are sealed, repositioned and permanently fastened.

Conventional Process		Proposed Process
Parts Measurement	End of Parts Measurement	Parts Measurement
		Parts Scanning
		Data Preprocessing
	Maximum Analysis Lead Time	FE Modelling
Pre-Assembly		Metamodelling
Gaps Measurement		Optimization
Shimming Fabrication	Beginning of Shimming Fabrication	Shimming Fabrication
Shimming Installation		Shimming Installation
Assembly		Assembly

Figure 7 - Conventional vs Proposed processes workflow

The proposed in-process approach starts with the component scanning after the critical dimensions are inspected. Then the scanned geometry is pre-processed to omit the positioning and clamping deviations induced by the scanning procedure. A nonlinear FEA based methodology is proposed in this work to recover the non-deformed geometry based on the scanned data, enabling its use in the predictive model. A nonlinear FEA predictive

method is established to represent the physical characteristics of the compliant assembly process and predict the derived distortions and stresses in the structure caused by the geometrical variations of the assembled components. In order to overcome the high computational cost of the nonlinear FEA predictive model, the number of variables of the problem is reduced by a methodology based on correlation analysis. A method based on the Response Surface Methodology (RSM) is then implemented to develop a surrogate of the nonlinear FEA model and reduce the computational time of the analysis. Finally, the search for an optimal solution is performed by a Multi-Objective Genetic Algorithm (MOGA) based method and the optimal shimming strategy is obtained from the derived set of non-dominated solutions, known as Pareto Front. The methodology was applied in a case study to demonstrate the accuracy and response time of the methodology.

The methodology was implemented using Static Structural and Design Exploration modules from ANSYS Release 19.1 [19]. The choice of the Ansys platform was driven by the capabilities of the package to handle modelling and optimization problems and the simplicity of working on a single development environment. Furthermore, as the methodology is intended to be used in industrial environments, an integrated and off-the-shelf solution is more suitable due to its quicker implementation, reliability and support accessibility.

The following sections detail the steps and considerations to implement the methodology and the solutions applied to overcome some of the modelling and optimization challenges listed as follows:

1. Accuracy of the scanned geometries
2. Accuracy of the predictive model

3. Shear locking problems in bending loads

4. High number of degrees of freedom

5. High dimensional problem

6. Computational cost and time consuming

3.1. Data Pre-processing

As the proposed in-process methodology relies on input data of as-produced parts to determine distortions and residual stresses, the geometries of the actual components are the reference for the predictive FE model.

As a consequence of equipment and tooling limitations, components are usually scanned or measured in conditions that differ from the way they are assembled. On the one hand, fixtures and clamps are used to constrain the parts, and on the other hand, input geometries for FE analysis need to be undeformed and load-free. Thus, this restriction prevents the use of the scanned data in the assembly analysis without being pre-processed. The effects are more critical for flexible parts that are more susceptible to distortions caused by the imposed boundary condition [20].
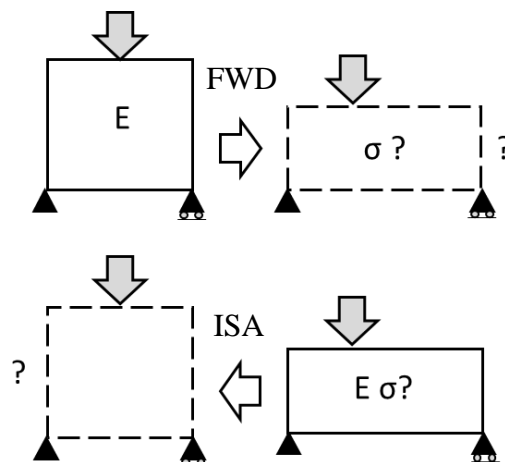
Figure 8 – Forward vs Inverse Solving Analysis - Adapted from [20]

The Inverse Solving Analysis (ISA) method (Ansys 2019 R3 [21]) is a nonlinear FEA solution that computes the undeformed geometry based on unknown stress/strain data, material properties, loads and boundary conditions of the input deformed geometry. The comparison of the initial and resulting condition of the forward and the inverse solving analysis is presented respectively in Figure 8. In the forward analysis (FWD), the initial geometry and its Young's module are the known inputs, while the deformed geometry and its stress σ distribution are the outputs of the simulation. In the ISA, besides the deformed geometry, the input data is composed of its Young's module, and the same boundary and loading conditions applied in the forward analysis or the scanning process, in real-world cases. The unknown output in the inverse analysis is the initial shape that derived the deformed geometry, i.e. the geometry with all deformations caused by the loadings and boundary conditions omitted. The nonlinear method is an iterative process that gives an updated reference geometry at the end of each substep based on the partial loads applied in the current substep. The resulting geometry of each substep, along with its stress and strains are incrementally analyzed with sequential load levels until the full loading is reached, and the recovered geometry is computed [20].

Reverse engineering techniques generate input geometries in real-world problems. The 3D scanning process of large volumes is usually performed by laser trackers that provide good accuracy within a short cycle time [22]. The process is basically executed in three phases: scanning, point processing, and application of geometric model development [23]. With the deformed digital geometry prepared, similar loadings and boundary conditions used during the scanning process are replicated on the FE model for inverse solving computation. Finally, the reference stress-free geometry generated from the analysis is

archived as an STL file, for instance, and used as the input model for the predictive analysis.

3.2.   Predictive Model

The predictive model aims to quantify the distortions and residual stresses developed in the assembly. Because of the large displacements required to comply with the components and the necessity of considering the contact in the model, the methodology was developed based on the nonlinear FEA approach. Despite the high computational cost and processing time, nonlinear compliant assembly models provide more precise outputs. The improvement in the results derives from the iterative update of the stiffness matrices while the loading conditions change during the assembly process. The contact effect is also crucial to ensure the accuracy of the model since it prevents penetrations among bodies causing displacements and stress errors, as shown in Figure 9.
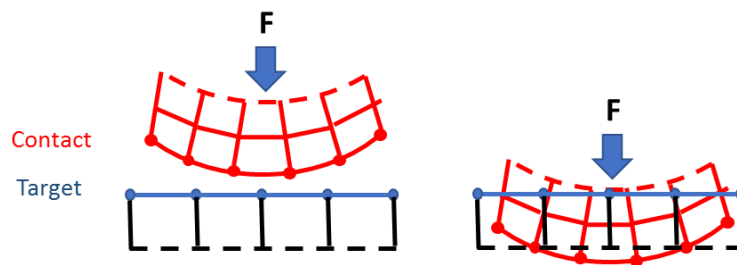
Figure 9 - Penetration - Adapted from [24]

The penetration can be prevented based on a method that establishes a relationship between the two contact surfaces to prevent them from passing through each other, i.e., to enforce contact compatibility [24]. The Pure Penalty contact method uses a contact interaction stiffness between the bodies, which is created by spring elements. As a result, the derived reaction forces induced by the springs prevent further penetration of the

surfaces in contact. Although, higher normal contact stiffness turns the penetration of one part in the other more difficult, stiffer contacts make the convergence harder to be reached as they lead to ill-conditioning of the global stiffness matrix. Thus, a trade-off between the model performance and output accuracy needs to be considered to set up the contact characteristics. Liao and Wang [25] analyzed the contact problem in sheet metal assembly variation, considering the friction force between the assembly surfaces. A nonlinear dimension variation analysis method was developed by establishing an elastic frictional contact model between the assembly surfaces and validated with physical experiments. In their study, the friction had minor influence in the numerical and physical experiments. Thus, following their conclusions, the proposed predictive model did not consider friction in contact modelling. According to Xie et al. [10], one of the main limitations of modelling contact in finite element models is convergence. Therefore, some measures to improve simulation stability were implemented. Mesh size, element stiffness, number of sub-steps for iteration, and other model parameters were considered and adjusted to increase the simulation performance.

In traditional assembly processes, fixtures or assembly tools are usually used to align parts, and therefore, their dimensions can interfere in the final state of the structure. In the present study, the influence of the jig variations was not considered as the assembly process was planned based on the jigless concept. Jigless or fixtureless assemblies rely on the diametrical and positional accuracy of two alignment holes per part interface [26]. The positive impacts of fixtureless assembly are the increased production flexibility, reduced non-recurring costs and development lead time.

Fastening forces have a significant effect on the stress distribution and distortions of assembled structures. The overall deformation is influenced by the rivet axial and radial pressures and the height of the driven head [27]. As the study focuses on the effects of the gaps and shimming distributions, the fastening mechanism considered only the axial forces produced by the fasteners, which is the main mechanism to join the components. Thus, longitudinal springs were used as elements to transmit the clamping forces as they are able to keep the loading direction towards the center of the coordinated holes despite any initial misalignment that may occur between them. Another simplification in the present study is that the assembly sequence was not considered as a variable in the analysis. Although different sequences might affect the alignment of the holes, it is assumed that eventual misalignments in real-world conditions could be corrected by reaming the holes before the installation of the fastener, which would prevent the increase of stresses and deformations in the structure. Based on the above considerations, the proposed predictive model was developed to carry all the parts and fastening forces simultaneously. These considerations reduced the complexity of the FE analysis since holes and fasteners were not required to describe the fastening mechanisms, allowing the study to focus on the modelling of the effects caused by distorted parts and on the methodology to search optimum assembly strategies.

In general, the geometries of compliant assemblies are very slender with mid to high aspect ratios. This condition might require a fine solid mesh to ensure a proper aspect ratio of the elements, which might increase the computational cost and processing time. Shear locking is a limitation of quadrilateral elements, caused by the presence of shear stresses in bending loads, preventing the model from computing deformations accurately. For solid

elements, the addition of layers over the height of the component may reduce the chances of locking issues. However, it can also lead to higher computational demand. In order to overcome these limitations, shell elements were selected to model the components of the assembled structure. In predominant bending problems, shell elements, with assumed displacement and transverse shear strain shape functions, are solutions to be considered to avoid shear locking issues in the analysis. Also, shell elements can better represent thin geometries as their performance is not affected by their thicknesses. Therefore, for the proposed application, shell elements are considered the most efficient modelling solution as they have less DOF in comparison to solid elements, and their derived mesh does not require further refinement to produce accurate results.

Shims are mechanical elements that are commonly used to fill remaining gaps in between surfaces that are not correctly mated. Its use prevents slipping movements and unpredicted shear loads due to the voids caused by the left gaps. It is assumed that the changes in the outputs of interest are derived from the variation of the compliant forces that consequently induce gaps in the structure that are ultimately filled with shims. Therefore, the shims' thicknesses are set as the main input variables since they drive the structure after the compliant forces are released, and the fastening forces are actuated. Since there are numerous possibilities to size and distribute the shims across the assembled structure that would affect the feasibility of the optimization analysis, it is recommended to determine the most critical shim locations and characteristics that more affect the chosen outputs of interest. The correlation analysis, presented in the next section, supports the definition of the most important input variables of the problem reducing its dimension for further analysis steps of the methodology.

3.3.   Correlation Analysis

The correlation analysis determines how strong the association is between two variables of interest. The importance of this procedure is because of the curse of dimensionality and the impacts on the computational cost and processing time, especially in the analysis of large nonlinear models. Therefore, by computing the correlation of inputs and outputs, it is possible to identify unimportant variables that could be ignored to simplify the analysis. Correlation analysis evaluates the linear relationship between two continuous variables, and Pearson's correlation is one of the most commonly used statistics to examine this relationship. The calculated correlation indexes can describe the strength, and the direction of the relationship that can be shown as null, positive or negative. The method evaluates a variation in one parameter associated with a proportional change in the other parameter. However, the correlation between two variables does not and cannot imply any causal relationship between them. The correlation coefficient value r can range from -1 to +1 and is given by Equation 6:

$$r = \frac{\sum_{i=1}^{n}(x_i - \bar{x})(y_i - \bar{y})}{\sqrt{\sum_{i=1}^{n}(x_i - \bar{x})^2}\sqrt{\sum_{i=1}^{n}(y_i - \bar{y})^2}} \tag{6}$$

where n is the sample size, x_i, y_i the individual sample points and $\bar{x}$, $\bar{y}$ the sample means.

The coefficient of determination R^2 represented in Equation 7 is the percent of the variation of the output parameter that can be explained by the linear or quadratic regression equation. It is also the ratio of the explained variation to the total variation. The coefficient of determination can range from 0 to 1.

$$R^2 \equiv 1 - \frac{\sum_{i=1}^{n}(y_i - f_i)^2}{\sum_{i=1}^{n}(y_i - \bar{y})^2} \qquad (7)$$

where n is the sample size, y_i the individual sample points, $\bar{y}$ the sample means and f_i the predicted values.

Correlation analysis occurs based on simulations of a random sampling of the design space. By default, Ansys uses the Central Composite Design sampling method. The method determines the overall trends of the model to determine the best sample points to reach an Optimal Space-Filling Design [28]. The convergence of the analysis is determined by the mean and the standard deviation that is evaluated according to the convergence frequency check set. The correlation analysis is considered stable when the mean difference is smaller than 1% from the previous step, and the standard deviation difference is smaller than 2%. If the Mean and Standard Deviation are stable for all output parameters, the correlation is converged [28]. After reaching convergence, the most relevant variables are selected based on the computed coefficients of correlation R and determination R^2 and the selected threshold criteria defined.

3.4.   Metamodelling

The response time of the proposed methodology is an important aspect to prevent delays in the production schedule. Thus, it is expected that the analysis time of the methodology shall be equal or lower than the time required to perform the pre-assembly and gap measurement in the conventional process. On the one hand, the use of nonlinear FE models increases the accuracy of the analysis, but on the other hand, their computational demand

and processing time might limit their direct use in optimization studies in industrial applications.

Metamodels are mathematical representations of physical models, widely used in simulation-based design optimization, used to reduce the computational cost of numerous expensive simulations [29]. Thus, they serve to approximate the response of high-fidelity numerical models in a more efficient way. The basic idea of meta-modelling is first to run a set of controlled computer simulation experiments. Then, based on the simulation results, a statistical model is established to describe the relationship between inputs and outputs [30]. This technique was applied to the nonlinear FE predictive model, considering the most relevant input variables selected from the parameters correlation analysis.

Response Surface Methodology (RSM) is a collection of statistical and mathematical techniques used in the development, improvement, and process optimization. The methodology has a significant application in the design, development, formulation and improvement of products and processes [31, 32]. RSM uses some simple basis functions to formulate the complexity of global objective and constraint functions in the design space. The methodology defines the effect of independent variables on the product or processes and generates a mathematical model. The fundamental relationship between the response and the input variables is given by Equation 8:

$$\eta = f(x_1, x_2, \dots, x_n) + \varepsilon \tag{8}$$

where η is the response, f is the unknown function of response, $x1, x2, \dots, xn$ are the independent variables, and finally, ε is the statistical error that represents other sources of variability not accounted for by f.

Because of the importance of metamodels in design space exploration and optimization, there was an interest in developing techniques to enhance their accuracy. The combination of individual metamodels as an ensemble algorithm can improve the accuracy of the predictions. Thus, an ensemble of metamodels for the approximation of response is expressed as a weighted-sum formulation [33] as presented in Equation 9:

$$\hat{y}_{ens}(x) = \sum_{i=1}^{N_M} w_i \cdot \hat{y}_i(x) \tag{9}$$

where $\hat{y}_{ens}(x)$ is the ensembled-predicted response, N_M is the number of metamodels in the ensemble, w_i is the weight factor for the ith metamodel, $\hat{y}_i$ is the response estimated by the *ith* metamodel, and x is the vector of independent input variables. The weight factors calculation is conditioned to Equation 10:

$$\sum_{i=1}^{N_M} w_i(x) = 1 \tag{10}$$

The weight factors are selected such that the metamodels with higher accuracy have higher weight factors [34]. Surrogates are fitted to function values at the sampled design points by determining the best weight factor values.

Genetic Aggregation is used to calculate the ensemble metamodels weights. The ensemble couples the appropriate methods in different types of metamodels that have their parameters set to create the first population while the next ones are obtained by cross-over and mutation [28]. Ansys Genetic Aggregation ensemble uses a combination of Polynomial Regression, Kriging, Support Vector Regression and Moving Least Squares to adjust the response surface to the design points better. The best weight factor values are determined through the minimization of the score and cross-validated values of the Root Mean Square

Error (RMSE) (Equation 11), the predicted residual error sum of squares (PRESS) of the

same Design Points cross-validated (Equations 12 and 13).

$$RMSE(\hat{y}_{ens}) = \sqrt{\frac{1}{N}\sum\nolimits_{j=1}^{N}\left(y(x_j) - \hat{y}_{ens}(x_j)\right)^2} \tag{11}$$

$$PRESS_{RMSE}(\hat{y}_{ens}) = \sqrt{\frac{1}{N}\sum\nolimits_{j=1}^{N}\left(y(x_j) - \hat{y}_{ens,-j}(x_j)\right)^2} \tag{12}$$

With:

$$\hat{y}_{ens,-j}(x) = \sum\nolimits_{i=1}^{N_M} w_i \cdot \hat{y}_{i,-j}(x) \tag{13}$$

where x_j is the *j-th* design point, $y(x_j)$ is the output value at x_j, $\hat{y}_{i,-j}$ is the prediction of the *i-th* response surface excluding the *j-th* design point, and N is the number of design points. Cross-validation error is a metric to prevent overfitting or selective bias in predictive models. It computes the error between the observed value and the predicted value for each point, excluding the DOE points associated with the observed value from the model. The cross-validation error is determined by dividing the dataset into K partitions, the model is trained on K – 1 partition, and the test error is predicted on the remaining partition k, the so-called K-Fold method. The process is called for k = 1,2…K, and the resulting error is averaged. For K=n, the process is known as Leave-One-Out Cross-Validation. As the Leave-One-Out method can be computationally expensive, Ansys uses 10-fold cross-

validation by default and switches to the Leave-One-Out method when the number of design points is small for 10-fold cross-validation [18, 28].

The quality of the metamodel is assessed by six Goodness of Fit parameters and their cross-validated scores. Besides RSME (Equation 11), the coefficient of determination R^2 (Equation 14), the maximum relative residual MRR (Equation 15), the relative root mean square error RRMSE (Equation 16) and the relative maximum absolute error RMAE (Equation 17) are computed to assess the model fitting for the learning points and its level of overfitting and bias [28].

$$R^2 = 1 - \frac{\sum_{i=1}^n (y_i - \hat{y}_i)^2}{\sum_{i=1}^n (y_i - \bar{y})^2} \tag{14}$$

$$MRR = \max_{i=1:N} \left(abs \left(\frac{y_i - \hat{y}_i}{y_i} \right) \right) \tag{15}$$

$$RRMSE = \sqrt{\frac{1}{N} \sum_{i=1}^{N} \left(\frac{y_i - \hat{y}_i}{y_i} \right)^2} \tag{16}$$

$$RMAE = \frac{1}{\sigma_y} \max_{i=1:N} \left(abs(y_i - \hat{y}_i) \right) \tag{17}$$

where y_i is the value of the output parameter at the ith sampling point, $\hat{y}_i$ is the value of the

regression model at the ith sampling point, $\bar{y}$ is the arithmetic mean of the values y_i, σ_y is

the standard deviation of the values y_i and N represents the number of sampling points.

Regarding the sampling strategies, the quality of fit is highly dependent on the DOE [35].

Latin hypercube designs are very well accepted in computer experiments because of the

flexibility related to data density and location [36]. The samples are allocated by dividing

the range of each variable into n equal intervals, and one value is selected from each

interval. The values for each variable are selected and coupled with the values of other

variables resulting in n vectors of variables. A full-quadratic model sample type was chosen

because it could generate the number of samples needed to create a full quadratic model

that can represent the physical model more accurately.

3.5.   Optimization

In general, the optimization of assembly processes has more than one objective function

to be improved simultaneously. In such problems, the objectives are usually conflicting,

and hence, there no exist single optimum solution.

Genetic Algorithms (GA) are based on the concept of natural evolution: the better

adapted the members, the more possibilities to transmit their characteristics to future

generations. The mutation of the elements is based on three main operators: Selection,

crossover and mutation operators. Additionally, random changes are applied in some

individuals to preserve the variation in the population [37]. Multi-objective genetic

algorithm (MOGA) tackles such problems by providing a set of solutions that cannot

improve more an objective function without degrading the conflicting ones. The so-called

non-dominated outcome lead towards a Pareto set, and the multi-objective optimization

algorithms push the search toward the Pareto-Front [37]. The multi-objective optimization problem can be generally described as Equation 18:

$$\min\bigl(f_1\left(x\right), f_2\left(x\right) \dots f_k\left(x\right)\bigr) \tag{18}$$

$$s.t.\, x\epsilon X$$

where $k \geq 2$ is the number of objectives, and X is the space of feasible solutions.

The feasible solution $x^* \epsilon X$ derives the objective vector $z^* := f(x^*) \epsilon \mathbb{R}^k$. A feasible solution $x^1 \epsilon X$ is non-dominated Pareto if $f_i\left(x^1\right) \leq f_i\left(x^2\right)$, for all $i \epsilon \{1, 2, \dots, k\}$ and $f_j\left(x^1\right) < f_j\left(x^2\right)$, for at least one index $j \epsilon \{1, 2, \dots, k\}$.

MOGA is a variant of Non-dominated Sorted Genetic Algorithm-II (NSGA-II). It ranks the solutions based on their domination and pushes the search towards the Pareto-front. NSGA-II spreads the solution across the Pareto-Front to avoid agglomerations. The Pareto ranking is derived from a non-dominant sorting method [28]. The Constrained Sampling method is applied as there exist defined parameters relationship. The initial sample is randomly selected by using a random number generator invoked internally by the Optimal Space-Filling (OSF) algorithm. MOGA generates a new population via cross-over and mutation. After the first iteration, each population is run when it reaches the defined number of samples. The convergence of MOGA is based either on the maximum allowable Pareto or convergence stability percentages, whatever is reached first. In the first criteria, the algorithm converges when the ratio of the number of Pareto points per number of samples per iteration reaches the set value. The convergence stability is calculated based on the population stability and the mean and standard deviation of the output parameters.

When a population is stable compared to a pre-defined value, the optimization is converged.

The optimum candidate points, selected from the Pareto-Front, are computed based on a decision support process, which is a goal-based, weighted, aggregation-based design ranking technique, that takes into consideration the importance level of objectives and constraints and the feasibility of the points [28]. Given n input parameters and m output parameters, the weighted objective function Φ is calculated according to Equation 19.

$$\emptyset \equiv \sum_{i=1}^{n} w_i N_i + \sum_{j=1}^{m} w_i M_j \tag{19}$$

where w_i and w_j are the weights of the outputs level of importance described in Table 1 and N_i and M_j, presented in Equations 20 and 21, are the normalized objectives for input and output parameters, respectively.

Table 1 - Output Importance Level x weight

Importance Level	Weight
Higher	1.000
Default	0.666
Lower	0.333

$$N_i = \left(\frac{|x_t - x|}{x_u - x_l}\right)_i \tag{20}$$

$$M_j = \left(\frac{|y_t - y|}{y_{max} - y_{min}}\right)_j \tag{21}$$

where x is the current value for input parameter i, x_t and y_t are the corresponding target values, y is the current value for output parameter j, x_l and x_u are the lower and upper values for input i respectively, and y_{min} and y_{max} are the lower and upper bounds for output parameter j [28]. Given UB and LB are the upper and lower bound respectively, the values x_t and y_t are determined according to Tables 2 and 3, respectively.

Table 2 - Decision Support Process - Input parameters

x_t	Objective
x	No Objective
x_l	Minimize
$0.5(x_l+x_u)$	Seek Target
x_u	Maximize

Table 3 – Decision Support Process - Output parameters

y_t	Objective	Constraint
y	No Objective	None
y_{min}	Minimize	Any
y_{t2}	Any	$value \leq UB \mid y \geq y_{t2}$
y	Any	$value \leq UB \mid y \leq y_{t2}$
y^*_t	Seek Target	Any
y	Any	$value \geq LB \mid y \geq y_{t1}$
y_{t1}	Any	$value \geq LB \mid y \leq y_{t1}$
y_{max}	Maximize	Any
y	Any	$LB \leq value \leq UB \mid y_{t1} \leq y \leq y_{t2}$
y_{t1}	Any	$LB \leq value \leq UB \mid y < y_{t1}$
y_{t2}	Any	$LB \leq value \leq UB \mid y > y_{t2}$

where y^*_t is the user-specific target, y_{t1} and y_{t2} are the constraints lower and upper bounds, respectively. The rating of each candidate design point is given by Equation 22, and its value ranges from +3 (Worst option) to -3 (Best Option).

$$Rating \approx \left(\frac{|\emptyset - UB|}{UB - LB} \times 6 \right) - 3 \tag{22}$$

4 -   Case Study – Data, Steps and Analysis

The case study evaluates the in-process method in a medium-to-large scale problem to determine the feasibility of obtaining accurate information within a reasonable response time. A hypothetic aluminum box (Figure 9) composed of four ribs, two spars and two skins were designed, and distortions were applied intentionally in some of the ideal geometries. This geometry was selected because of its geometrical similarities to some common aerostructures. The dimensions of the geometries were defined to exercise computational processing and memory allocation allowing proper evaluation of the performance of the method.
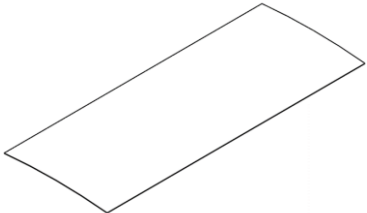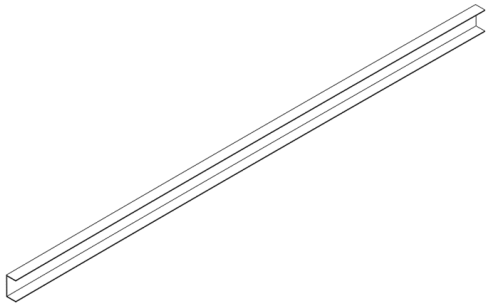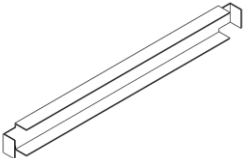
Figure 10 - Box with Distorted Components [19]

4.1.   Input Data

The box is composed of 4 Ribs, 2 Spars and 2 Skins. The basic dimensions of the box components are listed in Table 4.

Table 4 – Box parts - Basic dimensions

Part	Geometry	Thickness mm	Width mm	Length mm	Height mm
Skins		3	1000	2500	-
Spars		3	50	2500	100
Ribs		3	50	1000	100

Deformations were intentionally applied to the skins and spars, as shown in Figures 11 to 13, while the four ribs remained straight. The initial distortions were applied symmetrically on upper and lower skins and on the right and left spars.
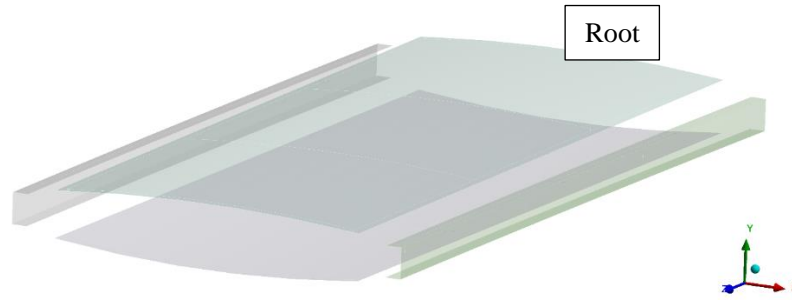
Figure 11 - Distorted Spars and Skins [19]
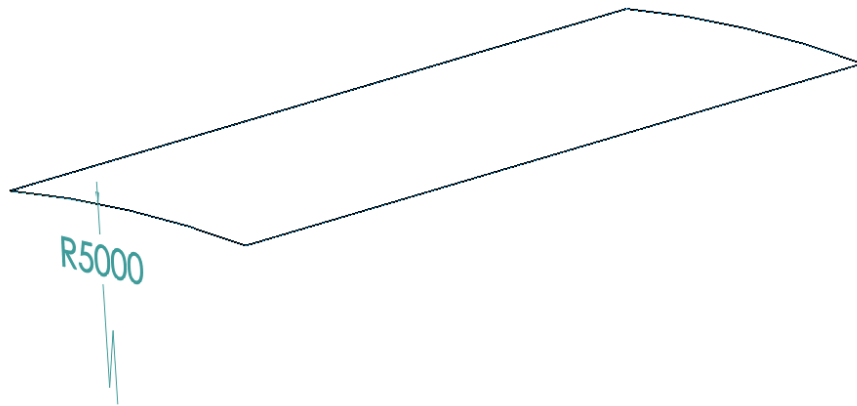
Figure 12 - Skin initial imposed distortion
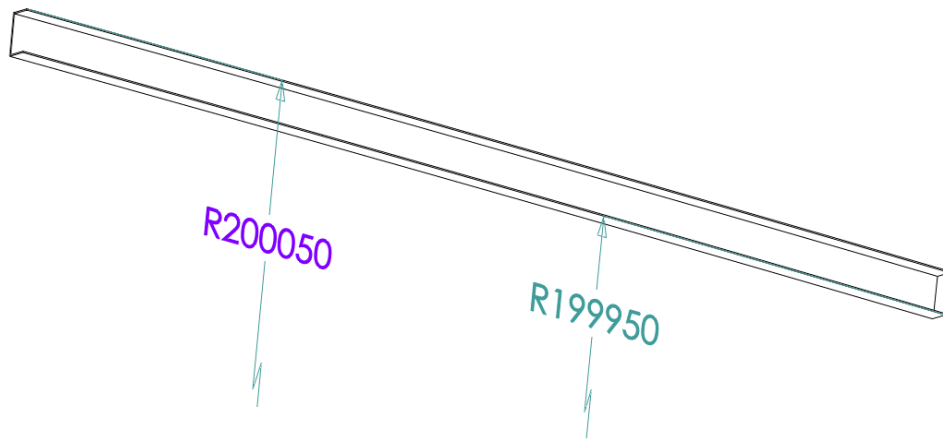
Figure 13 - Spars initial imposed distortion

A generic aluminum alloy was used to model the box components and shims. Table 5 depicts the properties of the chosen material, while Figure 14 shows the S-N curve for fatigue analysis.

Table 5 - Material Mechanical Properties [19]

General aluminum alloy (Ansys Materials Library)	
Density	2770 kg/m^3
Young's Modulus	71 GPa
Poisson's Ratio	0.33
Bulk Modulus	6960.8 MPa
Shear Modulus	2669.2 MPa
Tensile Yield Strength	280 MPa
Compressive Yield Strength	280 MPa
Tensile Ultimate Strength	310 MPa
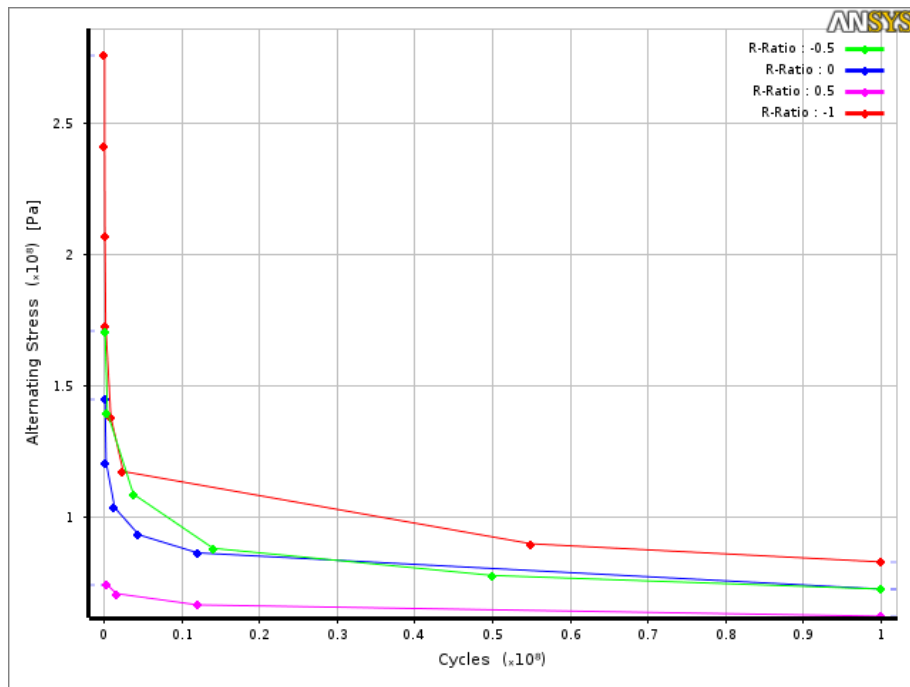
Figure 14 – General Aluminum alloy S-N curve - MIL-HDBK-5H, page 3-277 [19]

4.2. Simulation Steps

The simulation steps were implemented to allow the analysis to occur similarly to the actual assembly process. The relationship between the simulated and physical processes are shown in Table 6.

Table 6 – Simulation and Physical Assembly Steps

Step	Simulation Steps	Physical Assembly Steps
	Primary / connecting shims thicknesses updated	Shims are located and secured
0	Ribs are fixed through their web plane Spars are fixed through their root edges Skins are temporarily fixed through three vertices	Lateral Rib flanges are positioned on Spars webs Spars roots are located and fixed Skins are positioned on spars and ribs flanges Temporary fasteners are installed Auxiliary supports are used to keep alignment
1	Fasteners are activated	Fasteners are installed
2	Ribs and Skins are released	Auxiliary supports are removed
3	Gravity G and Force I are activated	Force I is applied

The loads and constraints applied in the structure in the 3-step analysis are illustrated in Figure 15. At the beginning of the analysis, the ribs are fixed through the web (A), the spars are fixed through the edges of the root (B), and the skins are constrained through three points (C-H). In the first step, the longitudinal springs are activated. Then the ribs and skins are released in the second step, allowing the structure to spring back. In the third step, the gravity is activated in -Y direction and the force I is applied in +Y direction at the web of Rib 4. In Tables 7 and 8, the type and location of the boundary conditions and loadings are detailed, respectively.
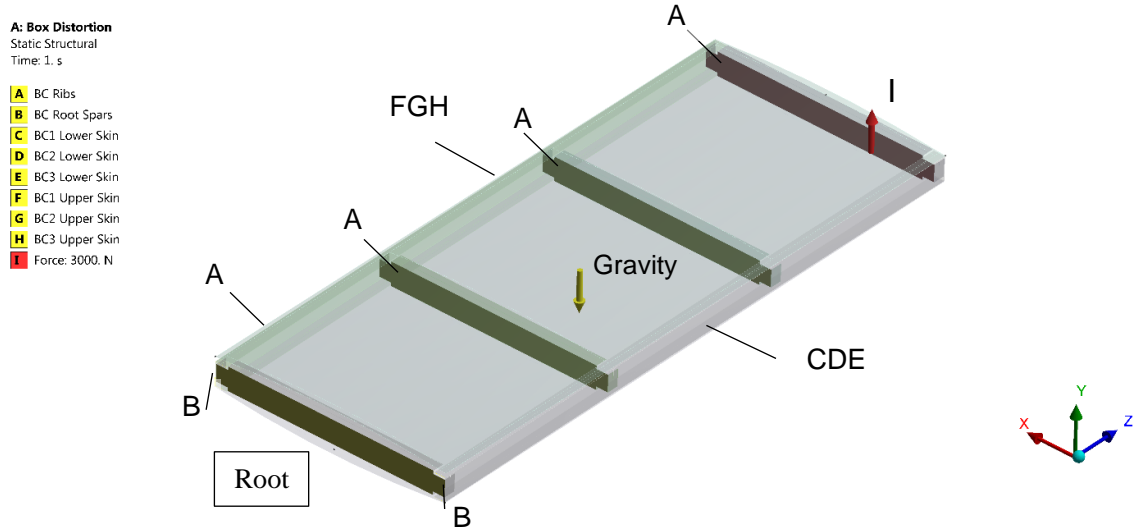
Figure 15 - Box - Loads and Boundary Conditions [19]

Table 7 - Simulation Boundary Conditions

Step	Components	Constraints	Constraint Location
	Ribs	Fixed (A)	Web - Surface
1	Spars	Fixed (B)	Root - Edges
	Skins	Displacement (C – H)	Fastener Location - Vertex
	Ribs	Free	-
2 - 3	Spars	Fixed (B)	Root - Edges
	Skins	Free	-

Table 8 - Simulation Loading Conditions

Step	Components	Loading	Loading Location/Direction
	All	Unloaded	-
1 - 2	Springs	Spring Preload	Fastener Location - Vertex
	All	Gravity	-Y
3	Springs	Spring Preload	Fastener Location - Vertex
	Rib 4	Force	Rib Web Surface - +Y

The 92 coordinated holes were omitted to reduce the complexity of the geometry and the mesh. Instead, they were replaced by the fastening points located at the center of the

omitted coordinated holes, as depicted as blue dots in Figure 16. The fastening points were then joined by pre-loaded longitudinal spring-tensions elements COMBIN14 that transmitted the clamping forces across their axis while keeping the load direction aligned to the reference points during the parts compliance. In this case study, the pre-load of all springs, which represents the clamping force created by the fasteners, was arbitrarily set to 1000 N. The spring stiffness was set to 20 N/mm in order to accommodate the necessary displacement to allow all fastening points across the structure to be joined with their pairs.

Figure 16 – The 92 Fastening Points / Longitudinal Spring locations (Blue dots) [19]

4.3. Analysis Considerations

The box in this case study was modelled with Ansys SHELL181 elements, which is suitable for analyzing thin to moderately thick shell structures with four-nodes and six degrees of freedom at each node [24]. A mesh sensitivity analysis was carried out to adjust the element size of the model, as detailed in Table 9 and Figure 17. The figure shows a

convergence trend after 16000 elements. Therefore, the mesh size configuration with 16904 elements was selected for the predictive model. Although the configuration with 18826 elements indicates to compute more accurate results, its computational time is 25% longer than the model with 16904 elements. The selected configuration was preferred in relation to the 16018 elements configuration due to the lower computational time and the finer mesh, which could contribute to the stability of the model during the DOE simulations.

Table 9 - Mesh Sensitivity Analysis Results

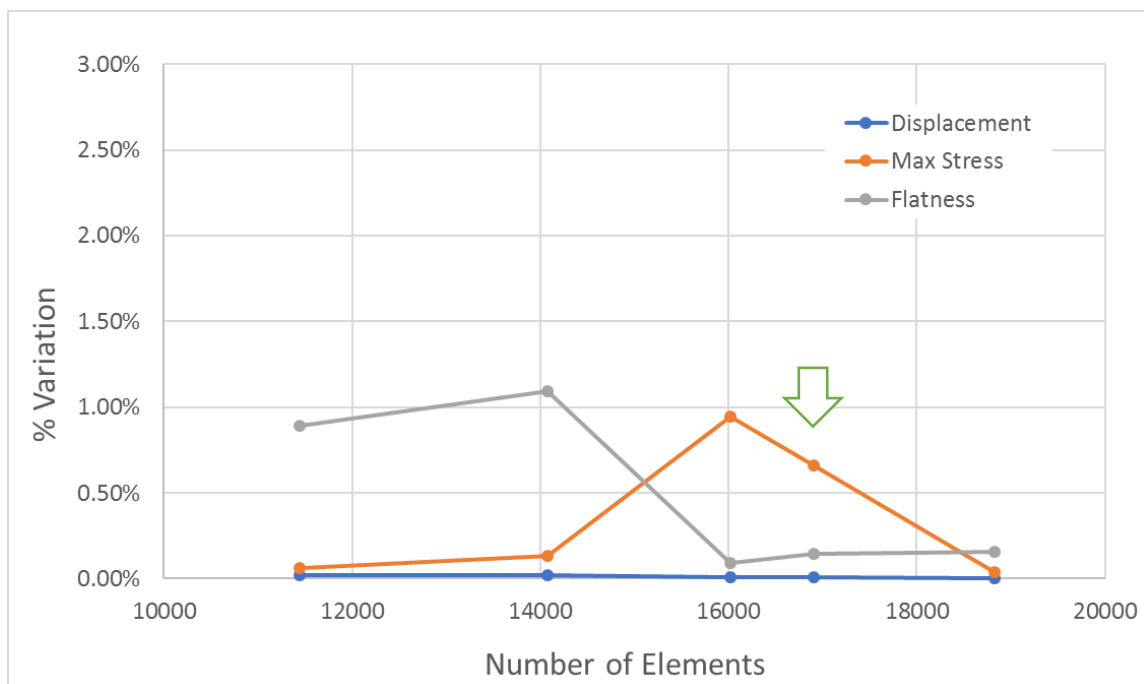| Elements	18826	**16904**	16018	14073	11445
Nodes	20746	**18776**	17811	15772	13072
Displacement [mm]	98.992	**98.992**	99.003	98.995	98.973
Max Stress [MPa]	204	**204.08**	202.74	200.84	201.11
Flatness [mm]	4.5378	**4.5307**	4.5372	4.5413	4.5914

Figure 17 - Mesh Sensitivity analysis and selected

The contact surfaces are deformable and have a 3D contour. Thus, CONTA174 and TARGE170 elements were selected to model the frictionless and bonded interaction between the mating surfaces. In order to prevent penetrations and allow a better convergence of the model, the normal stiffness factor was set to 10%, which is updated at each iteration of the analysis. Shims were set bonded to one of the components and frictionless to the second part allowing the relative movement of the parts until the springs are fully actuated. Table 10 lists the bodies and features in contact in the model and some of their characteristics.

Table 10 - Contact Pairs and Characteristics

Contact / Target	Contact Type	Element Type
Upper & Lower Skins (inner surface) Shims @ Spar caps	Frictionless	
Spars 1 -2 (Inner web) Ribs 1 – 4 (Lateral cap – outer surface)	Frictionless	
Upper & Lower Skins (Inner surface) Shims @ Ribs Caps (upper & lower)	Frictionless	CONTA174 TARGE170
Spars 1 -2 (Upper & Lower caps – outer surface) Shims @ Spar caps	Bonded	
Ribs 1 – 4 (Upper & Lower caps – outer surface) Shims @ Rib Caps (upper & lower)	Bonded	

Although the three outputs of interest were arbitrarily selected to illustrate the proposed methodology, they represent some of the most common requirements that can affect the functionality of aeronautical structures and should be controlled during the assembly process. The selected dependent variables, their optimization target and the importance level, are presented in Table 11.

Table 11 - Objectives and Priorities of the proposed Case-study

Variable	Target	Relevance
Fatigue Life	Maximize	High
Displacement	= Ideal Box tip displacement	Moderate
Flatness Defect	Minimize	Low

The load applied to compute the fatigue life was a zero-based cyclically force of +3000N without considering any mean stress theory. The displacement is measured at the tip of the spar 1 when the structure is loaded with the force (I) and the gravity (Step 3). The flatness defect is the maximum waviness amplitude measured from the movable medium surface on the upper skin just before the skins and ribs are released (Step 2).

The initial set of independent variables of the problem are the thicknesses of the 36 shims, depicted in green in Figure 18. The number of input variables was chosen to allow a proper evaluation of how the methodology handles several parameters to perform correlation analysis, metamodelling and optimization procedures. Shims were positioned across the entire structure to enable a complete sensitivity analysis of the response of the outputs of interest.
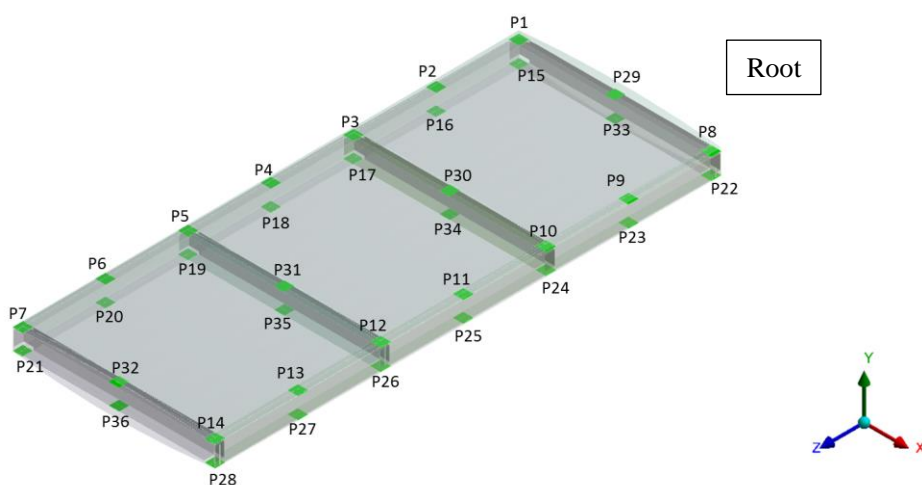

Figure 18 – Location of the 36 Primary Shims [19]

The spaces between two primary shims, omitted in Figure 18, are filled with connecting shims. The connecting shims are used to link the primary shims with a continuous surface creating support to prevent the mating areas from collapsing when the loads are applied. Primary shims are 50 mm x 50 mm Aluminum plates with thicknesses varying from 0.01 to 2.5 mm. Connecting shims are designed as 50 mm-width Aluminum stripes with different lengths and parallel or tapered depending on the thickness of the primary shims connected.

A parameter correlation analysis was performed to identify the shims with more influence on the parameters of interest. The samples of the 36 input variables were generated using Central Composite Design method. The coefficient of correlation r and coefficient of determination R^2 is calculated when the analysis got convergence. The criteria used to classify the input variables based on the coefficient of correlation r is presented in Table 12.

Table 12 – Coefficient of Correlation Ranges and Classification

Positive Range	Negative Range	Classification
0	0	No Linear Relationship
$0 \leq r < 0.2$	$-0.2 < r \leq 0$	Weak Correlation
$0.2 \leq r < 0.7$	$-0.7 < r \leq -0.2$	Moderate Correlation
$0.7 \leq r < 1$	$-1 < r \leq -0.7$	Strong Correlation
1	-1	Perfect Linear Relationship

Although coefficients ranging from 0 to ± 0.2 indicate a weak correlation, the present study adopted ± 0.2 thresholds to allow the model to obtain more information from the input variables and improve the accuracy of the metamodel. The 0.04 threshold of the coefficient of determination was set to allow that a minimum of 17 input variables could

be selected to represent the physical model. An additional input variable was included in the analysis to enable a simultaneous thickness variation of the less critical shims. Therefore, the modelling was performed with 18 input variables and the three outputs of interest.

A DOE based on the Latin Hypercube sampling method was set to generate the initial 190 design points. Genetic Aggregation was the chosen response surface methodology type because it automates the process to select, configure and generate the metamodel that best fits the learning points. Genetic Aggregation can build a response surface based on Full 2nd-Order Polynomials, Non-Parametric Regression, Kriging, and Moving Least Squares algorithms. Each shim thickness was arbitrarily bounded from 0.01 mm to 2.5 mm. The convergence of the Genetic Aggregation ensembled algorithm is based on the arbitrary tolerances depicted in Table 13.

Table 13 - Response Surface Methodology - Convergence criteria

Output	Target Tolerance
Fatigue Life	50000 cycles
Displacement	0.25 mm
Flatness Defect	0.5 mm

Additional samples could also be added manually or automatically to refine the model in case the convergence criteria were not reached. Finally, the metamodel quality is assessed through the analysis of the results of verification points and the calculation of Goodness of Fit parameters over the learning and cross-validated design points.

The optimization goal is to determine the thickness distribution of the shims that generates optimum outputs of interest for the assembled structure with distorted parts. The procedure is applied in the developed metamodel due to the computational cost and time

demanding of the nonlinear FE predictive model. The optimization problem can be described mathematically as the minimization of the functions shown in Equation 24.

$$(24)$$

$$\min \begin{cases} \Delta\delta = |a - F(X)| \\ -n = G(X) \\ f_{max} = H(X) \end{cases}$$

$$s.t. \{0.01 \leq X \leq 2.5mm$$

where $\Delta\delta$ is the difference between the displacements of the loaded tip box ideal assembly a (with ideal parts) and the assembly simulated F; n is the maximum number of cycles under a zero-based stress life analysis with no mean stress correction theory considered; f_{max} is the maximum flatness defect measured on the upper skin before the box is released to spring back and subjected to the loading and gravity, and X is the shims thickness vector. The importance level for optimization analysis was set high to the number of cycles, moderate to delta displacement at the box tip and low to maximum flatness, as presented in Table 11. MOGA was used in the analysis due to its capability of handling multi-objective problems. The optimization convergence criteria for the case study were arbitrarily set to 70% maximum allowable Pareto percentage and 2% maximum convergence stability with 3600 samples per iteration. Maximum Allowable Pareto Percentage criterion determines the maximum ratio of Pareto points per number of samples per iteration. Convergence stability percentage criterion determines when the population gets stable, based on the mean and standard deviation of the output parameters. The optimization converges when one of the two criteria converges to the set percentage.

A summary of the optimization parameters and convergence criteria used in the MOGA procedure is listed in Table 14.

Table 14 – Optimization Parameters and MOGA Convergence Criteria

Estimated Number of Evaluations	78400
Number of Initial Samples	10000
Number of Samples per Iteration	3600
Maximum Number of Iterations	20
Maximum Allowable Pareto Percentage	70
Convergence Stability Percentage	2

Since there exist differences between the surrogate and physical models, the selected points from the Pareto frontier need to be reassessed with the FE predictive model for verification of the outputs of interest and deliver a more accurate shimming map.

5 - Case Study – Results

This chapter presents the resulting distortions, stresses and fatigue outputs derived from the variation of shimming strategies in assembled structures. In addition, the analysis steps and demanded processing time are detailed to provide a more realistic sense of the impacts of the methodology in the real-world processes.

5.1. Data Pre-processing

The geometries and distortions used in the case study are hypothetical CAD models. Thus, the reference geometry did not require pre-processing to be used in the predictive model. However, to illustrate the Inverse Solving Analysis (ISA), the original distorted upper skin model was used to introduce the method. Thus, the original upper skin was virtually imposed on a horizontal surface (plane XZ) under the influence of gravity (Y direction), which represents a general scanning set up. As a result of the forward analysis, the displacements in the Y direction across the part extension were calculated and presented in Figure 19. The resulting geometry was then archived for the ISA.
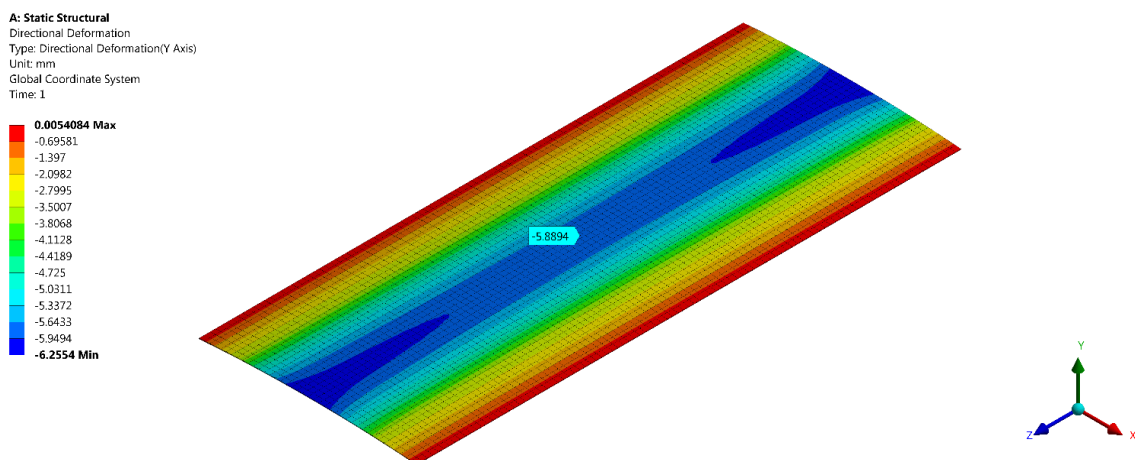

Figure 19 – Distorted Upper Skin under the influence of gravity [21]

The inverse solving method was then applied to the archived deformed geometry to recover the original distorted geometry. Thus, the boundary conditions and the gravity used to set up the forward analysis were reproduced on the archived model for the inverse solving analysis to be performed. After applying the method, a new geometry was obtained, as presented in Figure 20. As observed, the displacements caused by the gravity and boundary conditions on the original distorted geometry were almost entirely omitted by the opposite displacements generated with the inverse analysis. The displacements values and the absolute differences between both models are listed in Table 15.

Table 15 - Displacements derived from the Forward and Inverse Analysis

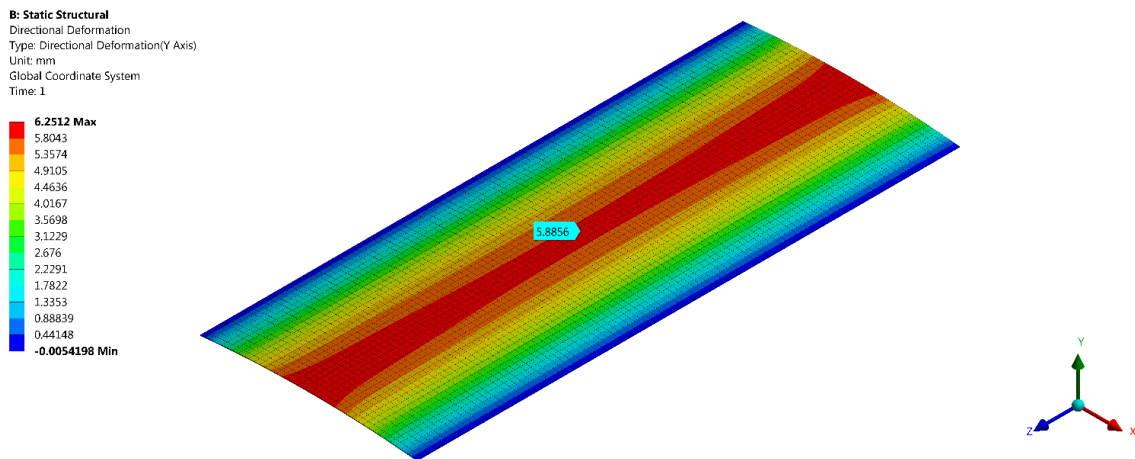|	Forward Analysis	Inverse Solving Analysis	Difference
Max Directional Y Displacement	6.2554 mm	6.2512 mm	0.0042 mm
Displacement Y @ Center	5.8894 mm	5.8856 mm	0.0038 mm

Figure 20 – Recovered geometry resulting from the ISA [21]

Both original and inverted geometries were superposed in order to determine the shape differences, as shown in Figure 21. As presented in the figure, the inverted geometry is found within the 0.05 mm tolerance range of the original CAD upper skin. The orange lines along the top upper skin surface represent deviations caused by the facets of the generated STL files. The resulting recovered geometry is then archived to be used as a reference geometry in the FE predictive analysis.
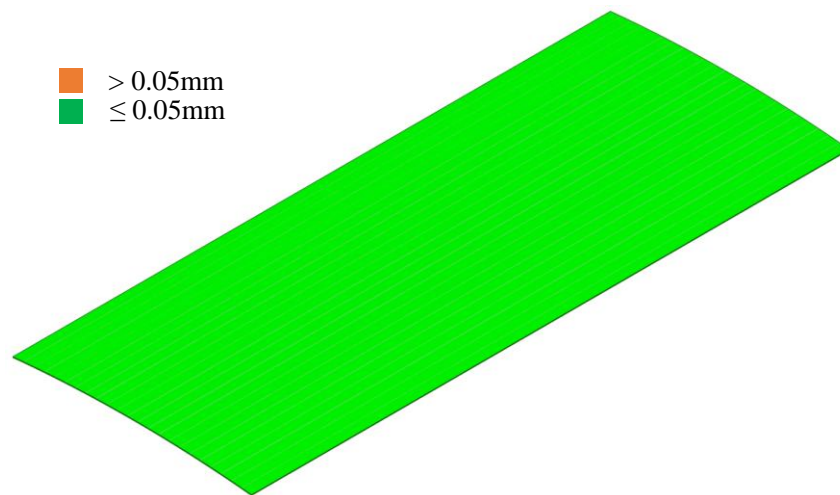

Figure 21 - Deviation Analysis - Original vs ISA [21]

5.2.   Preliminary Analysis - Ideal Parts

The analysis with ideal parts (nominal dimensions) determines the performance baseline for the assembled structure. The results derived from this study were used to compare with the outputs of the structure composed of non-ideal parts under the influence of different assembly strategies. Table 16 summarizes the outputs derived from the simulation of the ideal parts assembly.

Table 16 - Outputs Summary - Ideal Parts Assembly

Assembly Type	Displacement [mm]	Flatness Defect [mm]	Max Von Mises Stress [MPa]	Fatigue Life [cycles]
Ideal Parts	100.65	0.625	203.8	1.365 E7

After the application of the force (3000N) and activating the gravity, the tip center of spar 1 (orange circle) displaced 100.65 mm upwards, as presented in Figure 22.
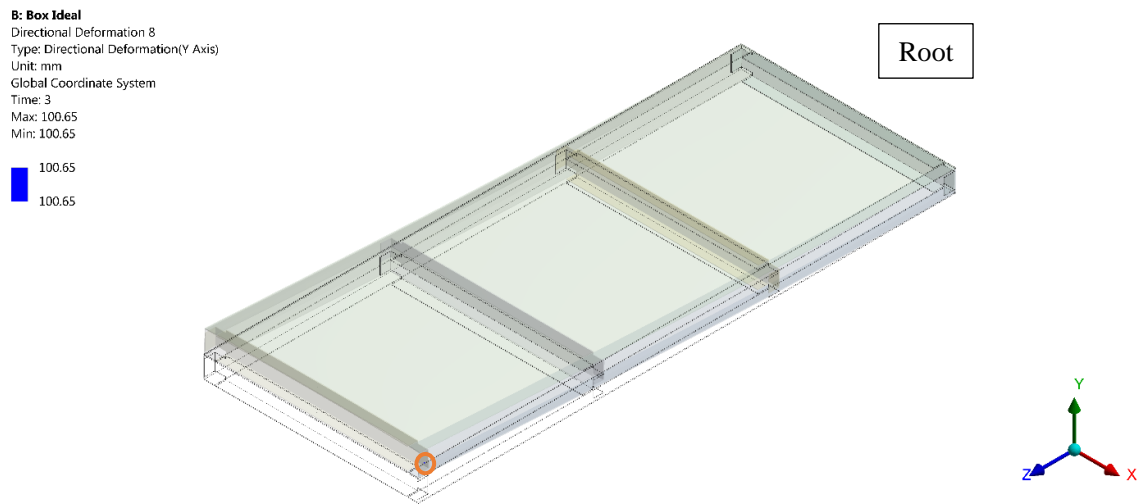

Figure 22 - Ideal Box - Displacement in the Y direction in Step 3 [19]

The flatness defect on the upper skin, shown in Figure 23, was measured at the end of Step 2, i.e. after the ribs and skins were released and before the loads were applied.
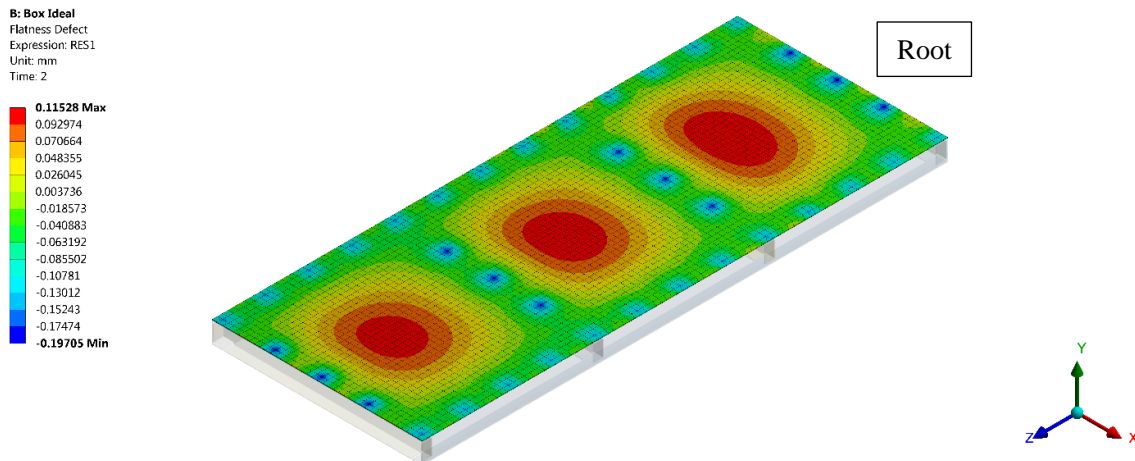
Figure 23 - Ideal Box - Flatness Defect in Step 2 [19]

The von Mises stress distribution, along with the assembled structure after the application of force and gravity, is depicted in Figure 24. As observed, the higher stresses are concentrated in the root spars areas.
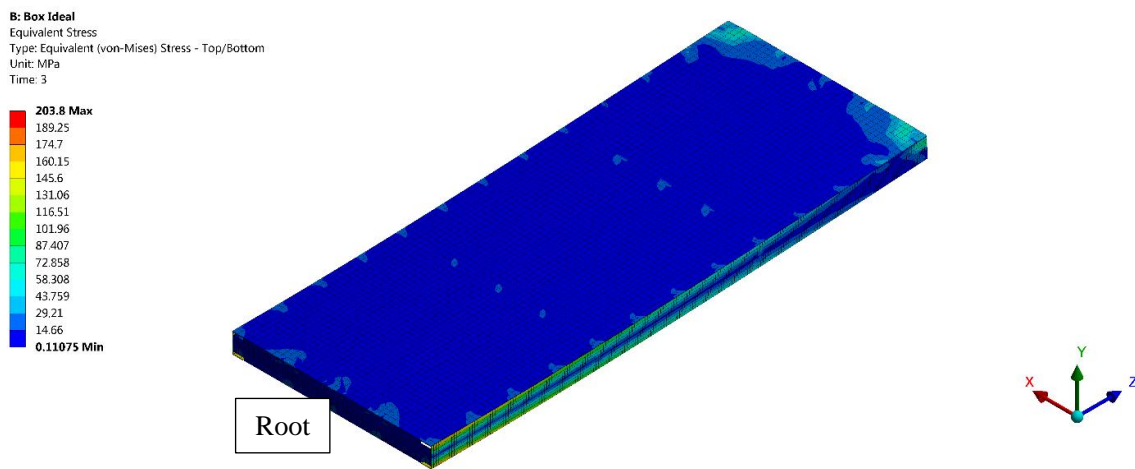

Figure 24 - Ideal Box - von Mises stress in Step 3 [19]

For better visualization, Spars' geometries were isolated and plotted in Figures 23 and 24.

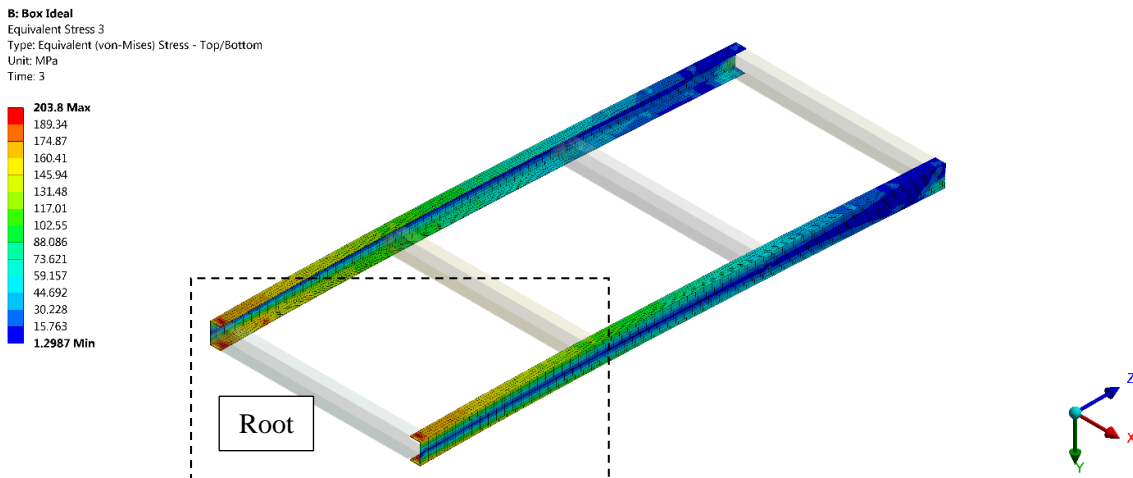Figure 25 - Ideal Box - Maximum von Mises stress Spars in Step 3 [19]
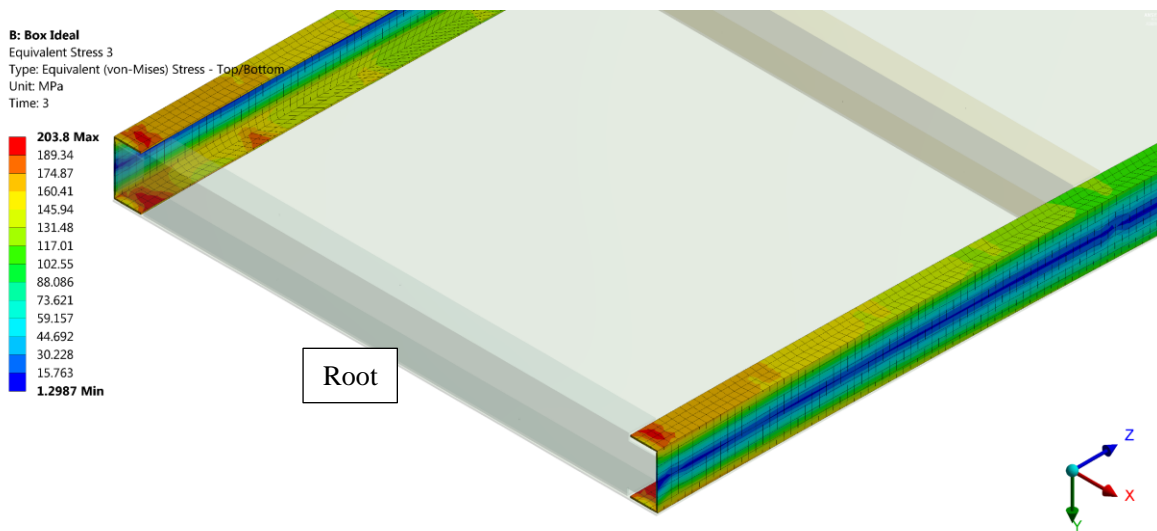

Figure 26 - Ideal Box – Maximum von Mises stress Root Spars in Step 3 – Detail [19]

The minimum fatigue life for the ideal box, derived from the zero-based cyclical load of the force I, was calculated for the set boundary conditions. Its location coincides with the location of the maximum von Mises stress, as shown in Figure 27.
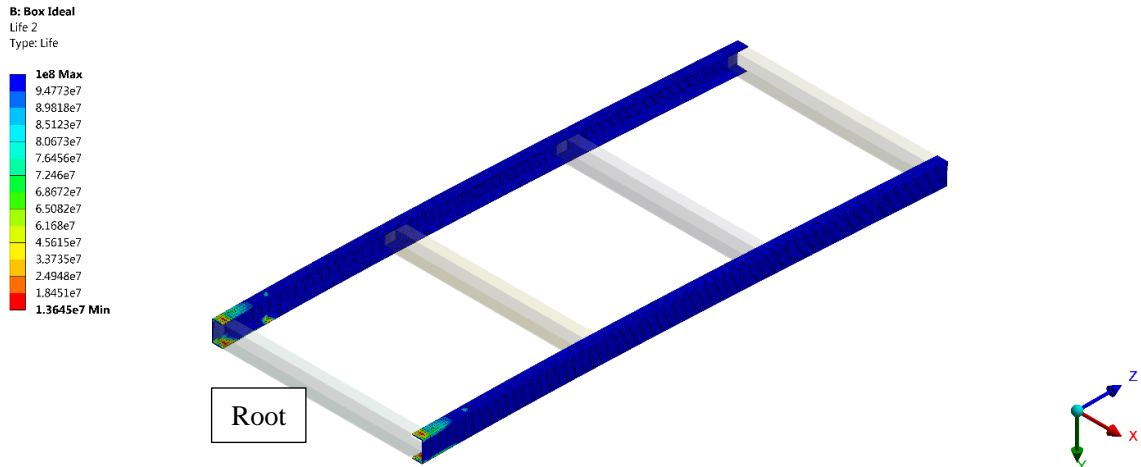
Figure 27 - Ideal Box - Fatigue Life at 0-3000N cyclical loading [19]

5.3.   Preliminary Analysis - Non-Ideal Parts - No Shims

The non-ideal parts were assembled without shims, and their mating surfaces were forced to be matched. This configuration represents the less expensive assembly condition since it does not require the fabrication and installation of shims. Table 17 presents the calculated outputs, and the results are plotted in Figures 28 to 33. For the distorted parts selected, there was no significant variation in maximum von Mises stress and fatigue life compared to the ideal-parts assembly. The displacement of the structure of the non-ideal parts is 1.65% lower than the ideal-parts structure when the force I is applied at the Rib 4. An increase of almost 400% in the flatness defect output is found in the shimless structure assembled with non-ideal parts.

Table 17 - Outputs Summary – Non-Ideal Parts Assembly (Shimless)

Assembly Type	Displacement [mm]	Flatness Defect [mm]	Max Von Mises Stress [MPa]	Fatigue Life [cycles]
Ideal Parts	100.65	0.625	203.8	1.365 E7
Non-ideal Parts Shimless	98.992	3.123	204.08	1.343 E7
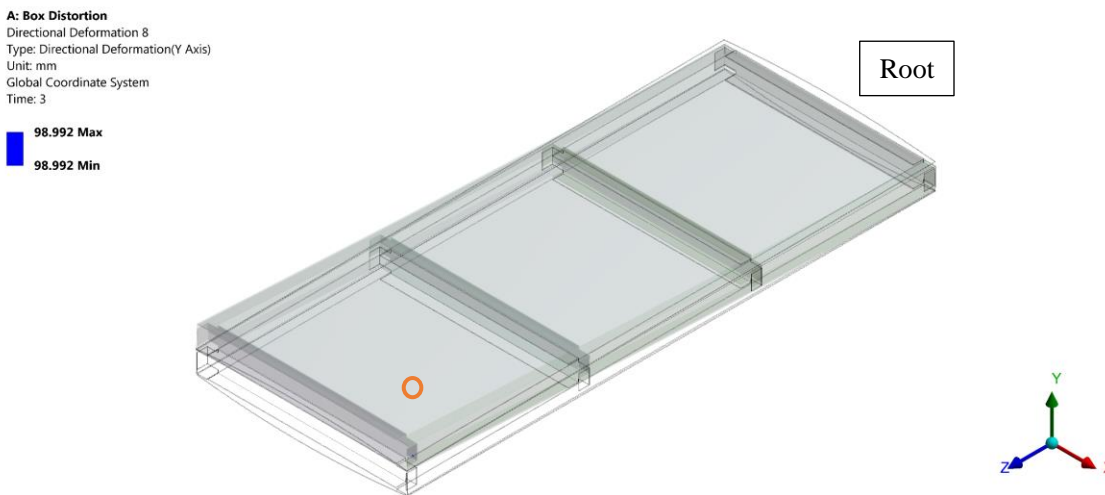
Figure 28 – Non-Ideal (shimless) - Box Tip Displacement in Step 3 [19]
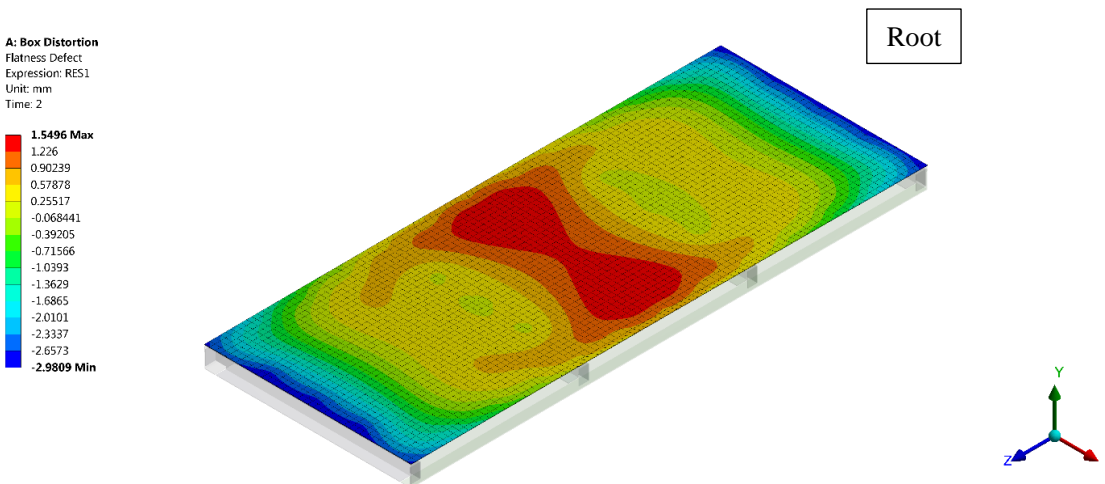
Figure 29 – Non-Ideal (shimless) - Upper Skin Flatness Defect in Step 2 [19]
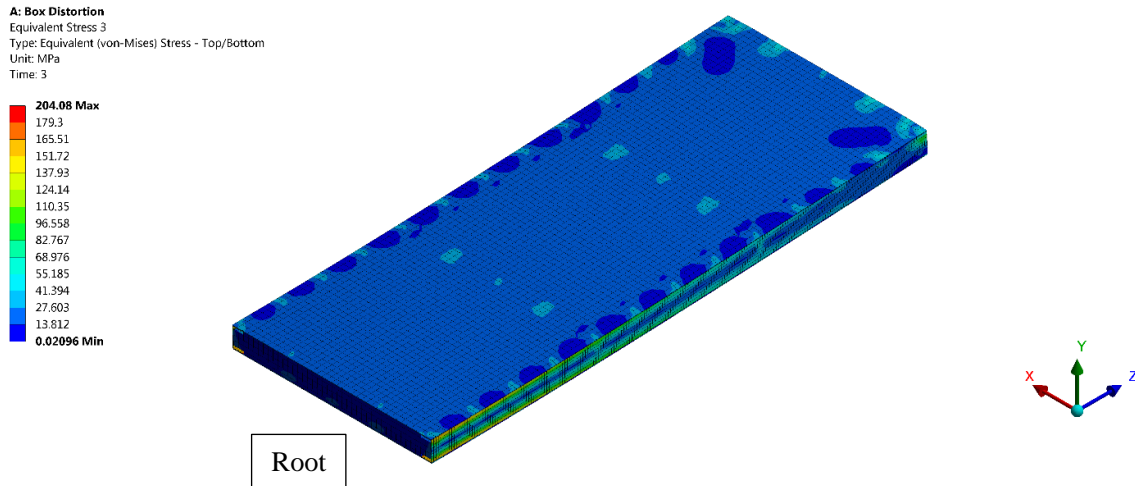
Figure 30 – Non-Ideal (shimles) - Box von Mises Stress in Step 3 [19]
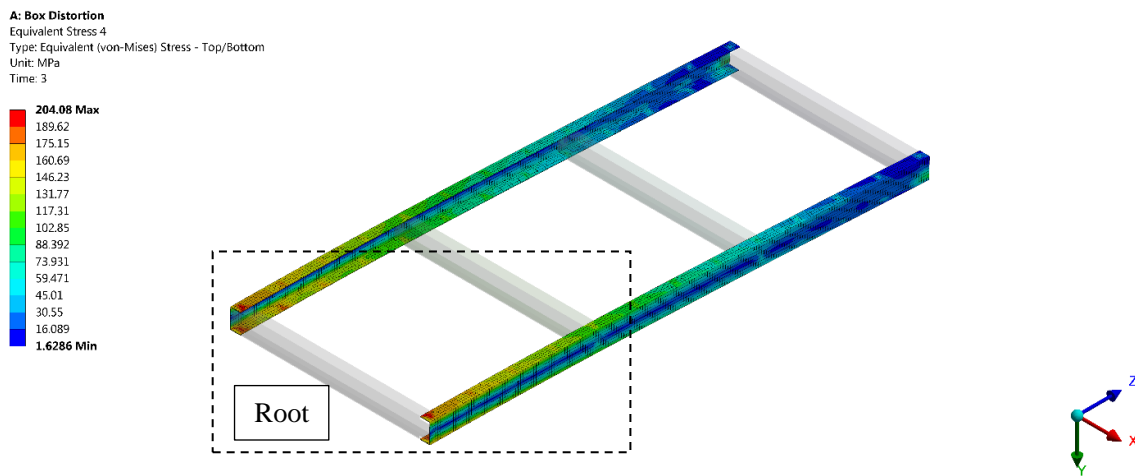
Figure 31 – Non-Ideal (shimless) - Spars von Mises Stress in Step 3 [19]
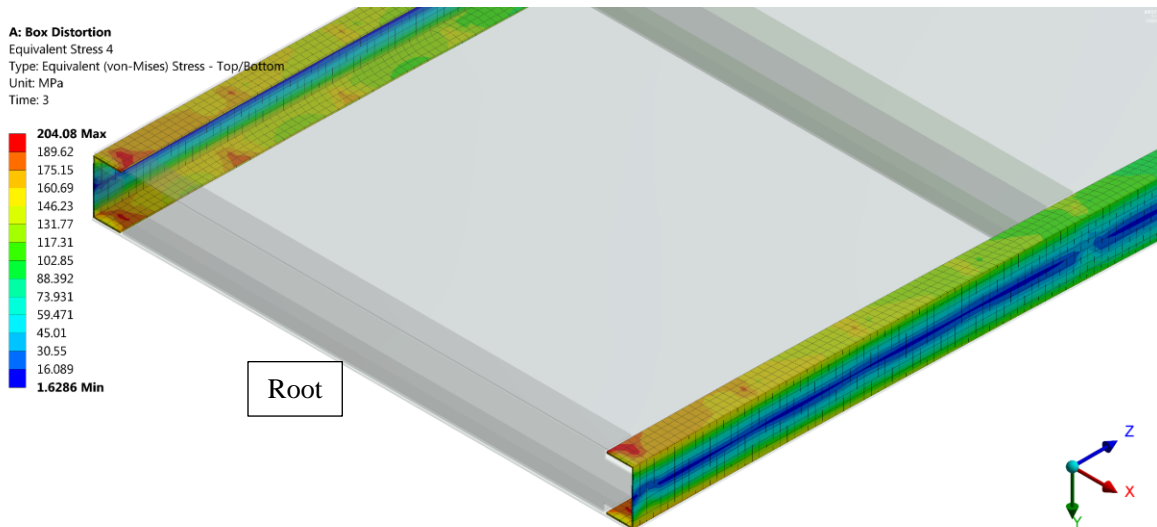
Figure 32 – Non-Ideal (shimless) – Spars Max von Mises stress in Step 3 - Detail [19]
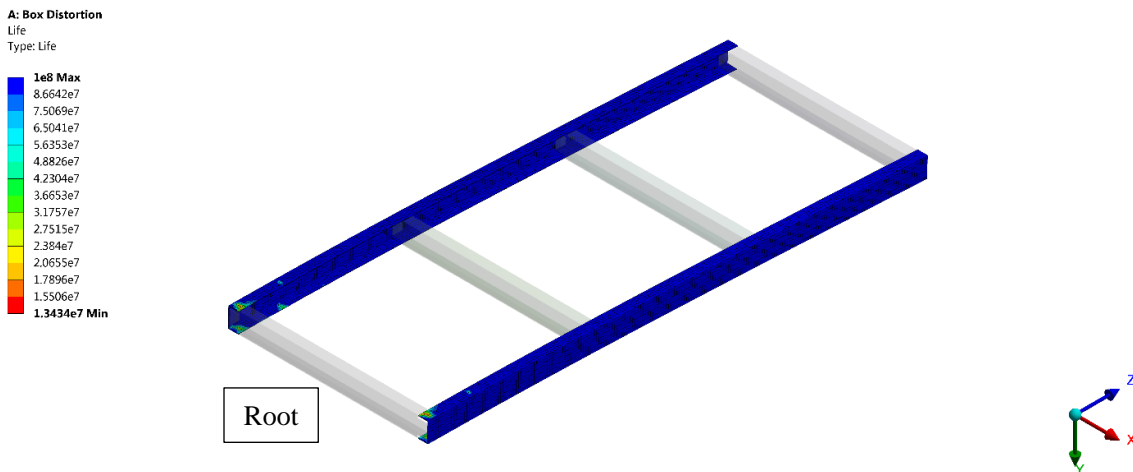
Figure 33 – Non-Ideal (shimless) - Spars Fatigue Life at 0-3000N cyclical loading [19]

5.4.   Correlation Analysis

The correlation analysis converged with the computation of 185 design points. According to the set coefficients of correlation (20%) and determination (4%) thresholds

presented in Section 4.3, the 17 shimming locations selected for the metamodel development were: P1, P2, P4, P8, P11, P12, P13, P15, P16, P18, P22, P23, P26, P27, P28, P33 and P36, as depicted in Figure 34.
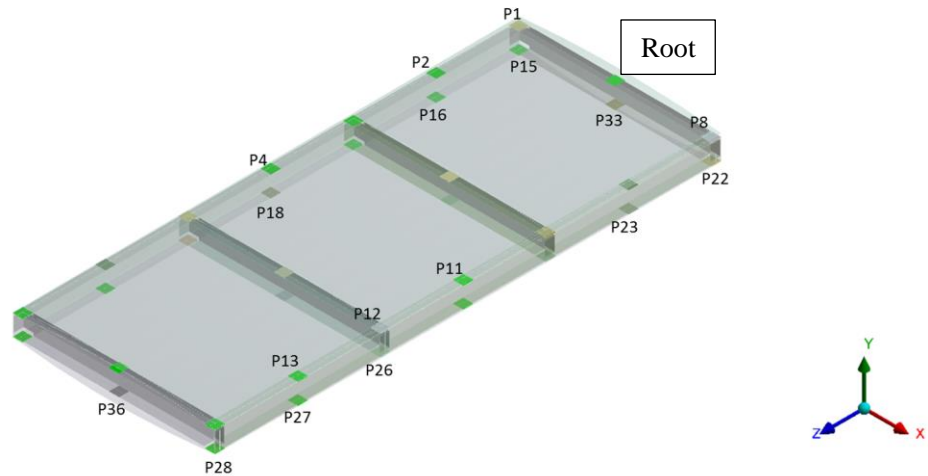
Figure 34 - Selected Input Variables based on the Correlation Analysis [19]

Table 18 presents the coefficients of correlation and determination of the 36 input variables related to the three outputs of interest. The highlighted values represent the coefficients of correlation and determination that are more significant than the set thresholds in relation to any output of interest. Figures 35 and 36 describe the distribution of the coefficients of correlation and determination of the 36 input parameters and their position related to the threshold lines. All independent input variables that surpassed the threshold value of either the coefficient of correlation or determination were considered significant for the metamodelling step.

Table 18 - Coefficients of Correlation and Determination of the 36 Shims

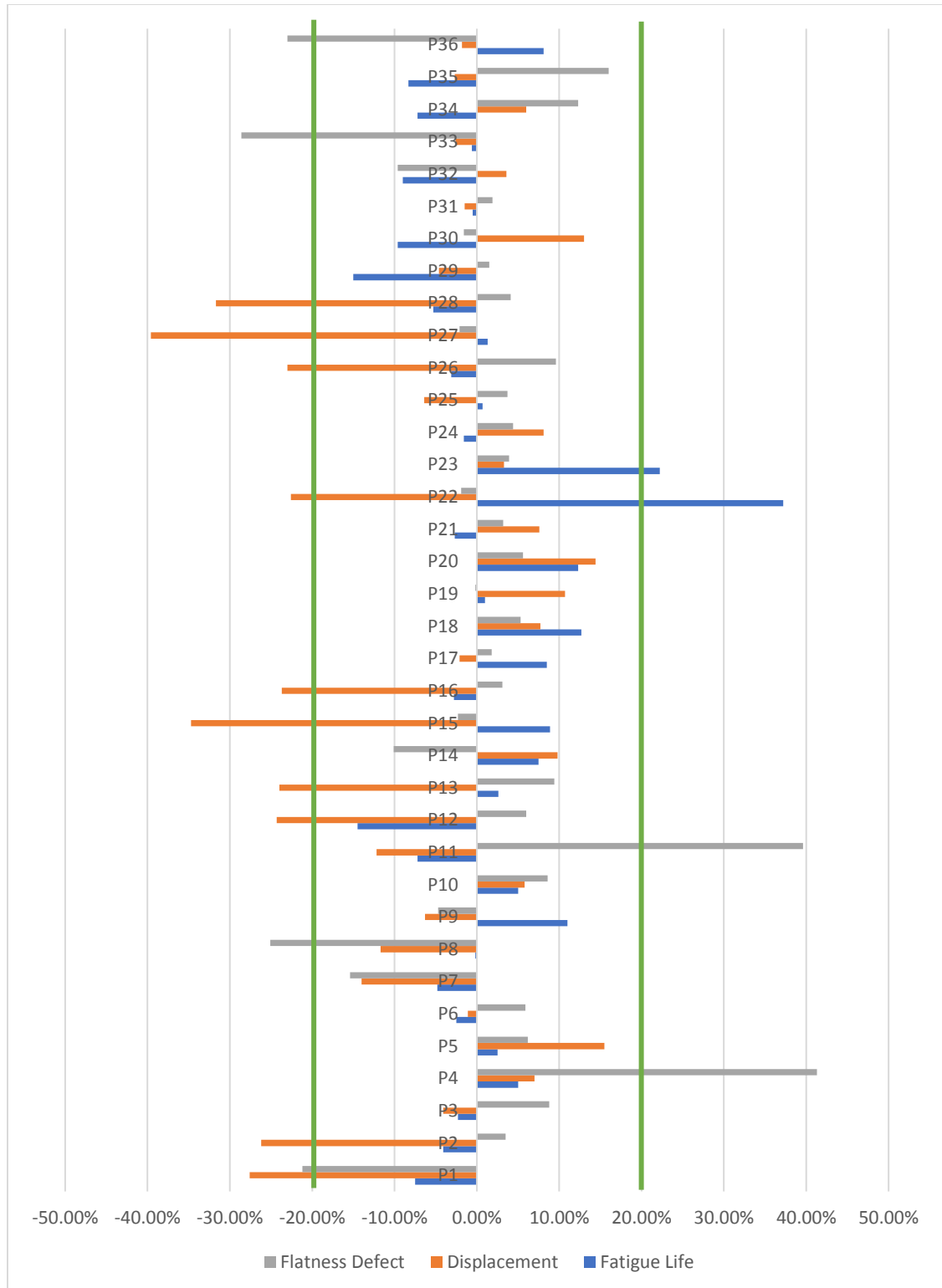| Shim ID	Coefficient of Correlation r			Coefficient of Determination R^2		
	Fatigue Life	Displacement	Flatness Defect	Fatigue Life	Displacement	Flatness Defect
P1	-7.5%	-27.6%	-21.2%	2.3%	7.8%	5.6%
P2	-4.1%	-26.2%	3.5%	4.5%	7.0%	0.2%
P3	-2.3%	-4.1%	8.8%	0.5%	1.3%	0.8%
P4	5.0%	7.0%	41.3%	0.4%	0.7%	17.1%
P5	2.5%	15.5%	6.2%	0.1%	2.5%	1.4%
P6	-2.5%	-1.1%	5.9%	0.2%	0.0%	1.3%
P7	-4.8%	-14.0%	-15.4%	0.9%	3.5%	2.8%
P8	-0.2%	-11.7%	-25.1%	0.0%	1.5%	6.5%
P9	11.0%	-6.3%	-4.7%	2.5%	0.6%	1.0%
P10	5.0%	5.8%	8.6%	0.3%	0.4%	0.9%
P11	-7.2%	-12.2%	39.6%	0.5%	1.5%	16.1%
P12	-14.5%	-24.3%	6.0%	2.3%	6.5%	1.3%
P13	2.6%	-24.0%	9.4%	0.2%	5.9%	0.9%
P14	7.5%	9.8%	-10.1%	1.2%	1.8%	2.3%
P15	8.9%	-34.7%	-2.3%	5.8%	12.2%	6.4%
P16	-2.8%	-23.7%	3.1%	0.7%	5.7%	3.5%
P17	8.5%	-2.1%	1.8%	0.8%	2.5%	0.0%
P18	12.7%	7.7%	5.3%	4.7%	0.6%	4.7%
P19	1.0%	10.7%	-0.2%	0.0%	1.3%	0.2%
P20	12.3%	14.4%	5.6%	3.8%	2.1%	0.6%
P21	-2.7%	7.6%	3.2%	0.1%	0.6%	0.3%
P22	37.2%	-22.6%	-1.9%	26.1%	5.3%	1.3%
P23	22.2%	3.3%	3.9%	5.0%	0.1%	0.4%
P24	-1.6%	8.1%	4.4%	0.1%	0.9%	2.0%
P25	0.7%	-6.4%	3.7%	0.3%	0.9%	0.1%
P26	-3.1%	-23.0%	9.6%	0.2%	5.6%	2.2%
P27	1.3%	-39.6%	-2.1%	0.0%	17.5%	0.7%
P28	-5.3%	-31.7%	4.1%	0.9%	10.5%	1.8%
P29	-15.0%	-4.6%	1.5%	2.3%	1.1%	0.0%
P30	-9.6%	13.0%	-1.6%	0.9%	2.0%	0.0%
P31	-0.5%	-1.5%	1.9%	0.2%	0.8%	0.2%
P32	-9.0%	3.6%	-9.6%	0.8%	0.4%	0.9%
P33	-0.6%	-2.6%	-28.6%	1.5%	0.2%	8.2%
P34	-7.2%	6.0%	12.3%	0.5%	0.6%	1.5%
P35	-8.3%	-2.7%	16.0%	2.1%	0.5%	3.1%
P36	8.1%	-1.8%	-23.0%	1.9%	0.0%	9.4%

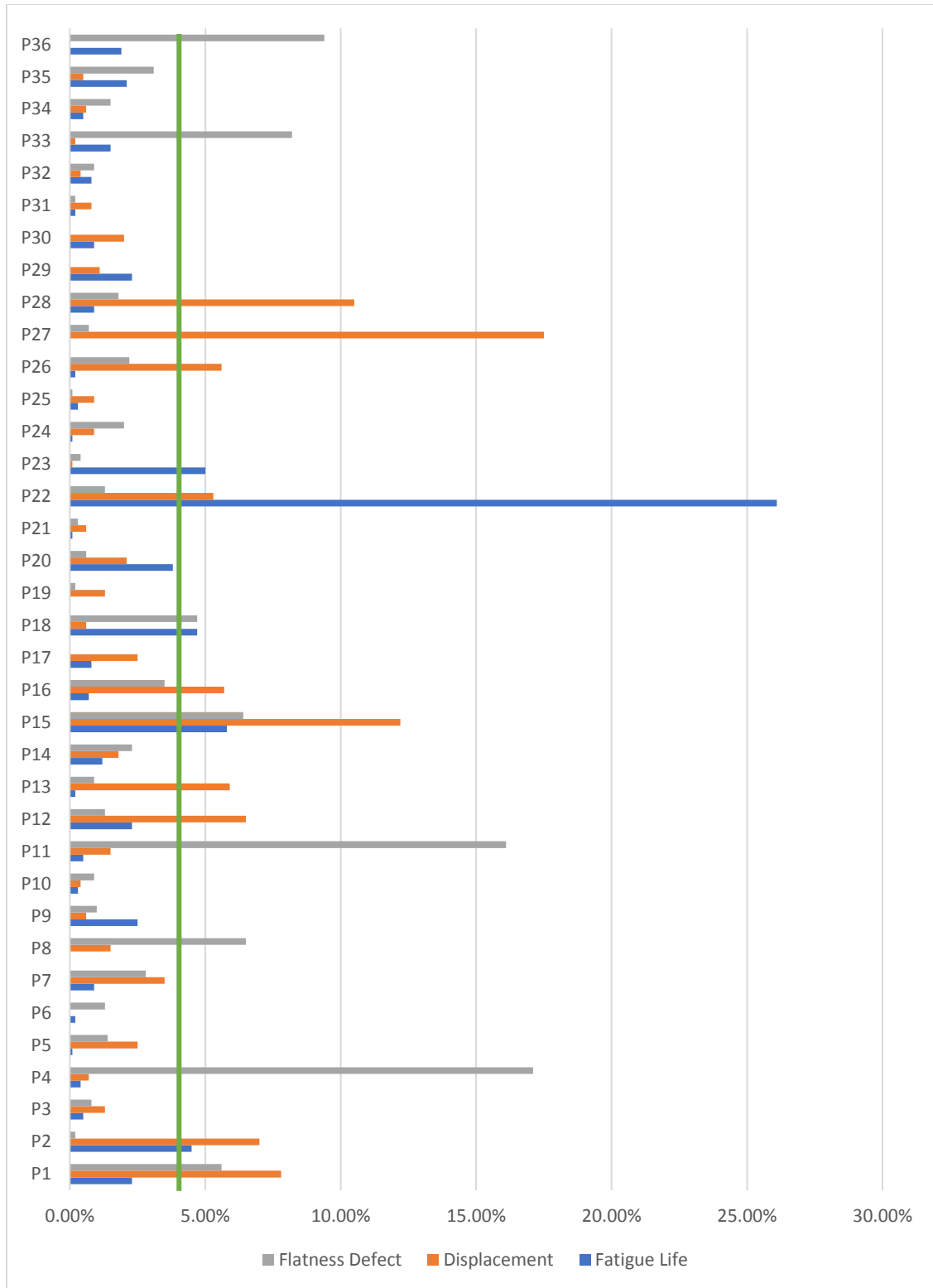Figure 35 - Coefficients of Correlation *r* of the 36 shims and Thresholds

Figure 36 - Coefficients of Correlation R^2 of the 36 shims and Threshold

5.5.   Metamodelling

17 out of the total 36 shims were selected from the parameters correlation analysis and set as the independent variables. One additional variable was designated to represent the thickness variation of the 19 remaining shims that will vary simultaneously. Therefore, the 17 + 1 input variables and the 3 outputs of interest were used to develop the RSM of the metamodel. The convergence of the RSM analysis is constrained by the error/tolerance ratio. The criteria used for this case study was based on the convergence tolerances presented in Table 11 and the predicted error/tolerance ratio calculated on the learning points, which was set to 1.0.

As the RSM did not converge with the initial 190 design points, 75 new refinement points were added to improve the quality of the response surface until the maximum predicted error/tolerance ratio was reached, as demonstrated in Figure 37.
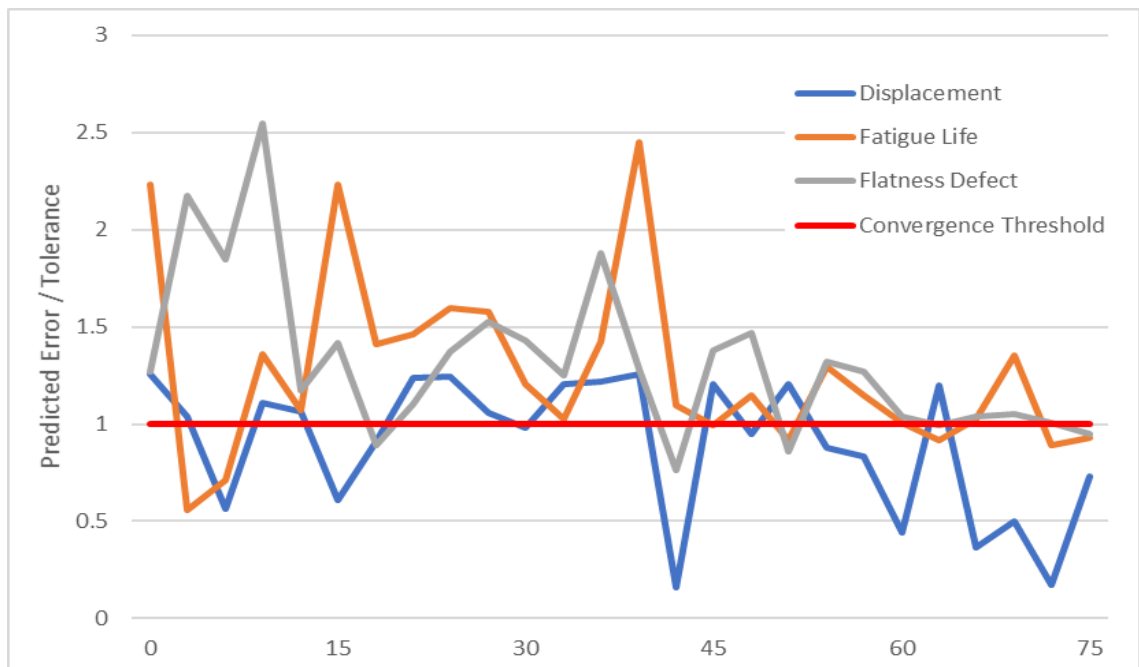

Figure 37 – RSM Convergence chart of the 75 Refinement Points

The derived ensembled genome of the response surface model after convergence is detailed in Table 19.

Table 19 - Ensemble Genome of the RSM model

Members [35]	Weight
Kriging – Bessel – Isotropic – Pure Quadratic	23.491%
Kriging – Thin Plate Spline – Anisotropic - Linear	15.086%
Kriging – Damped Sin – Isotropic – Pure Quadratic	23.56%
Polynomial Regression – Full Quadratic	9.3381%
Polynomial Regression – Full Quadratic	9.249%
Kriging – Thin Plate Spline – Isotropic – Pure Quadratic	19.277%

The quality of the metamodel was assessed by the goodness of fit quality parameters, presented in Table 20.

Table 20 - Goodness of Fit parameters of the RSM

		Displacement	Fatigue Life	Flatness Defect
R^2	Learning Points	1	1	1
	Cross-Validation	0.96128	0.73086	0.81177
RMSE	Learning Points	6.9169E-9	0.13301	6.3585E-8
	Cross-Validation	0.046028	3.3728E+5	2.7285E-1
RRMSE	Learning Points	0	0	0
	Cross-Validation	0.046296 %	2.442 %	4.7185%
MRR	Learning Points	0	0	0
	Cross-Validation	0.39604 %	6.8308 %	15.165 %
RMAE	Learning Points	0	0	0
	Cross-Validation	168.05 %	148.83 %	157.12 %

The plots with the predicted and observed values for the three outputs of interest, based on the learning and verification points, are shown in Figures 38 to 40.
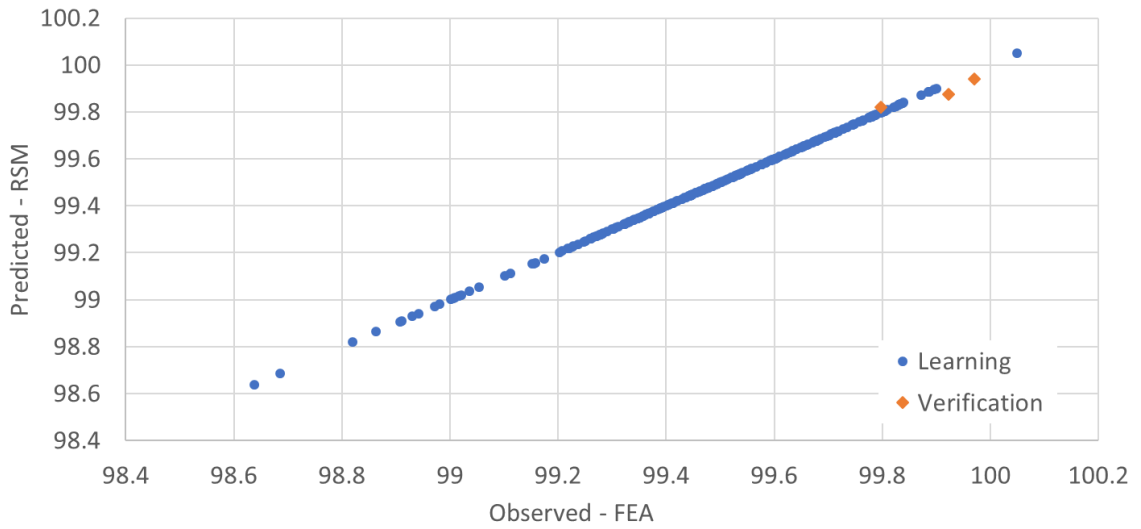
Figure 38 - Predicted vs Observed chart - Learning and Verification points – Displacement
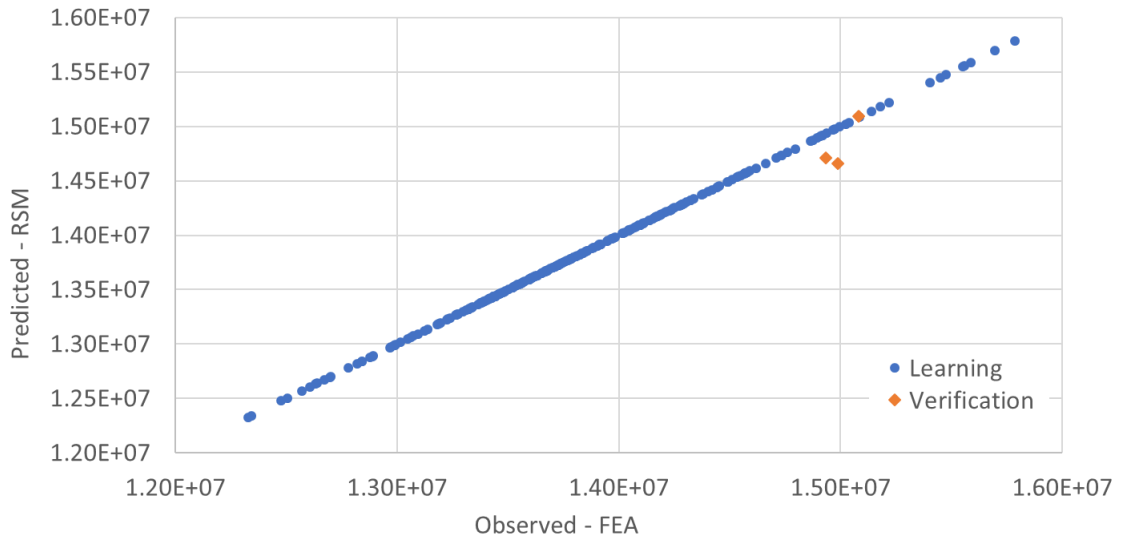

Figure 39 – Predicted vs Observed chart - Learning and Verification points – Fatigue Life
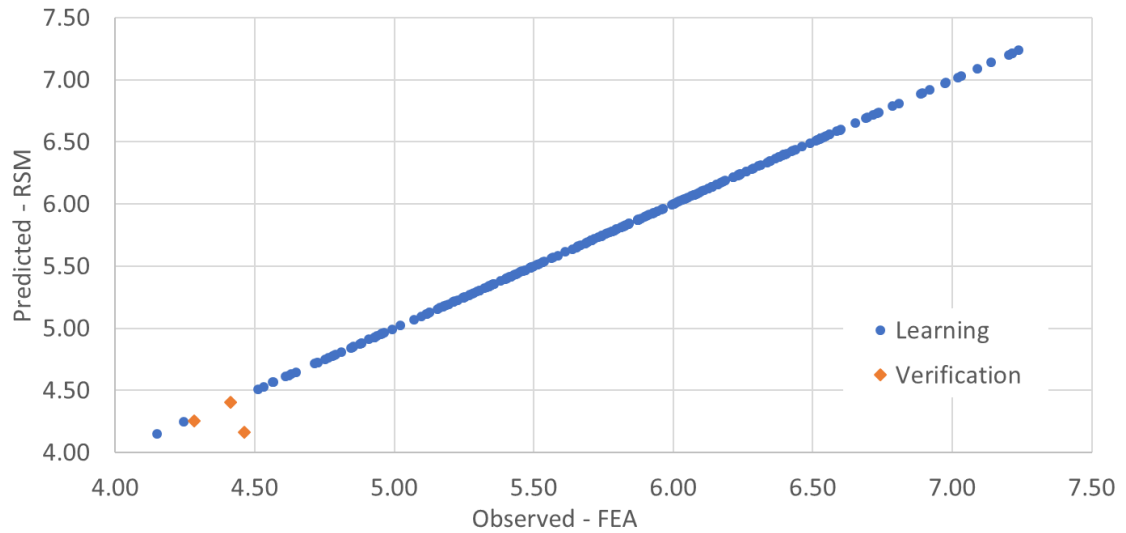
Figure 40 - Predicted vs Observed chart - Learning and Verification points – Flatness Defect

Although the values of the parameters for the learning points indicate a good fit of the response surface, their high cross-validated values, especially for Fatigue Life and Flatness Defect outputs, suggest some overfitting and bias issues in the metamodel. However, since the errors found in the verification points are relatively low and within the set tolerances presented in Table 13, and only the MRR and RMAE parameters present relatively high errors, it is likely that the results from the cross-validation analysis reflect a high dependence of the metamodel to the design points rather than overfitting and bias.

To illustrate the response behaviour of the outputs of interest by the variation of some input parameters, the Fatigue Life, Displacement and Flatness Defect responses surfaces are presented in Figures 41 to 43. The input variables used in the charts correspond to the shims with the highest coefficients of determination R^2 computed in the correlation analysis.
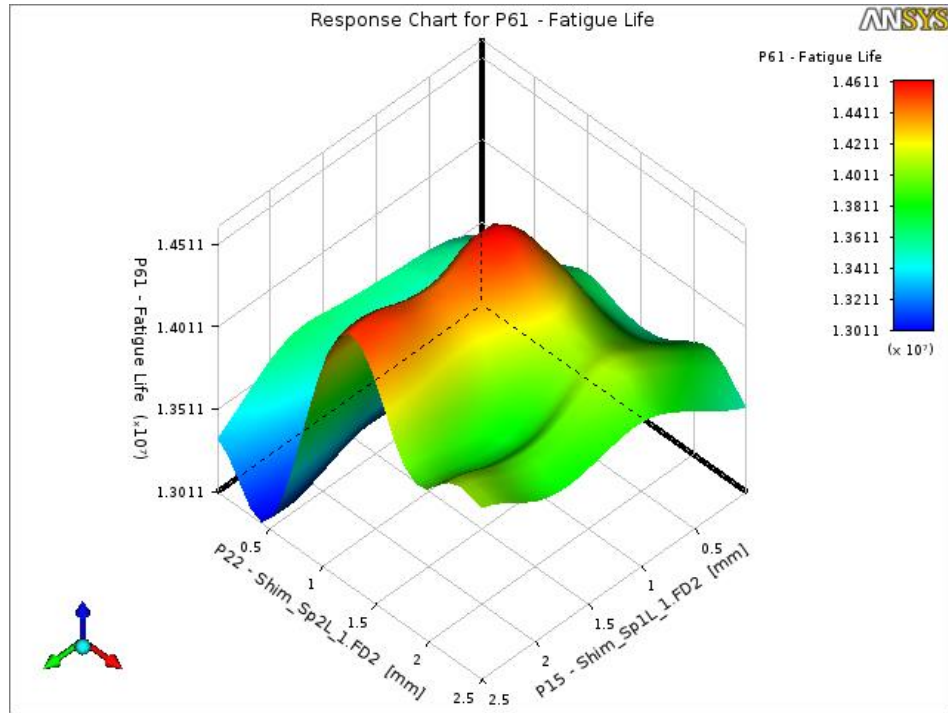
Figure 41 - RSM - Fatigue Life [cycles x 10^7] for P15 and P22 [19]
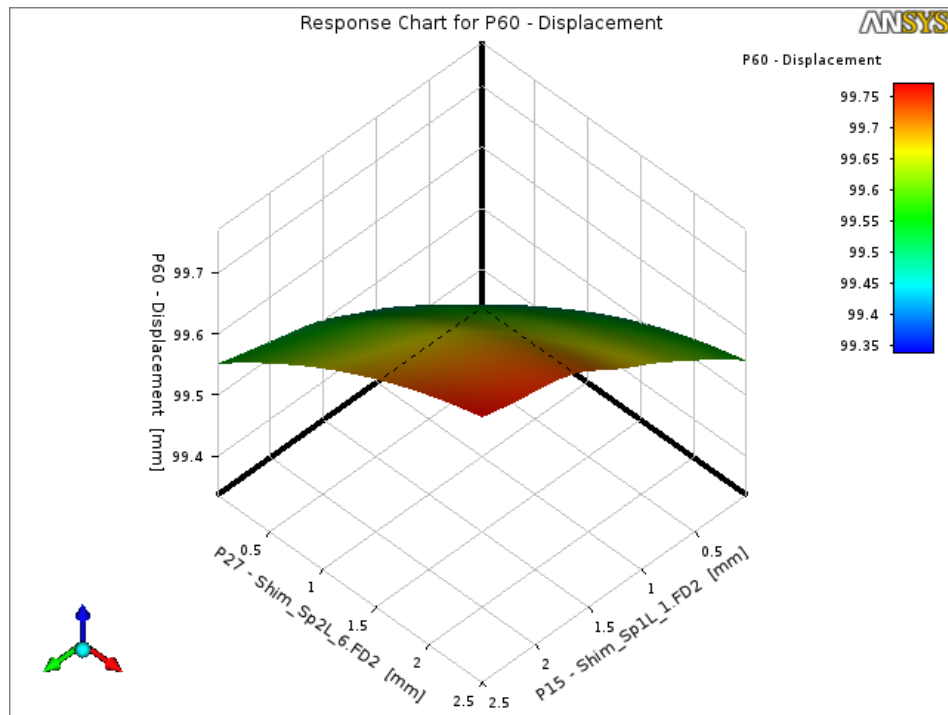
Figure 42 - RSM – Direct Deformation [mm] for P15 and P27 [19]
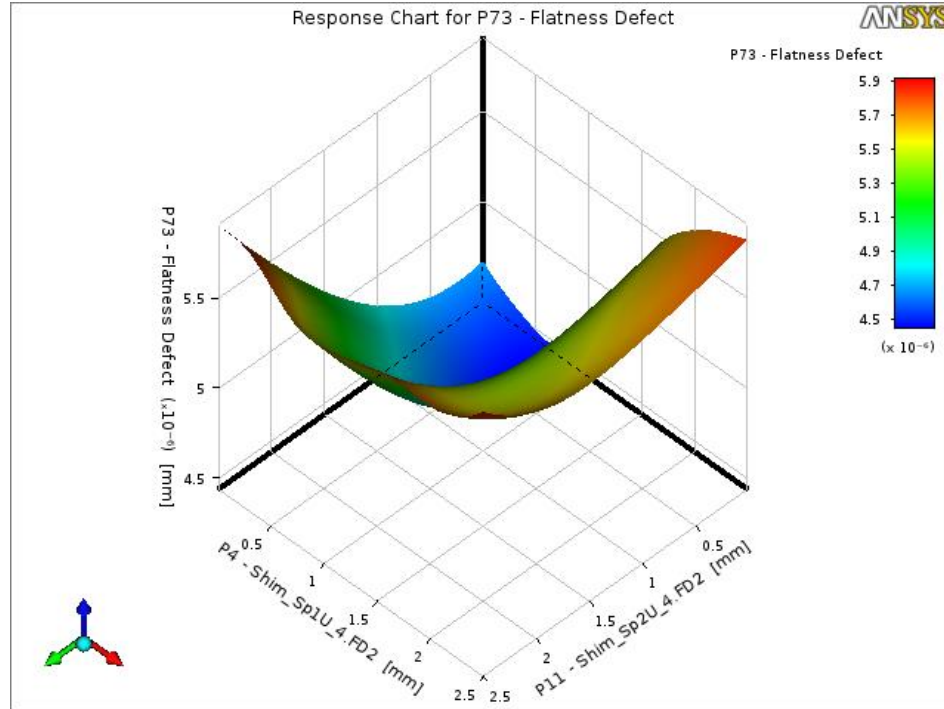
Figure 43 - RSM - Flatness Defect [mm] for P4 and P11 [19]

The local sensitivity chart presented in Figure 44 shows the impact of a single input parameter on the output parameter, i.e., the change of the outputs based on the variation of the 18 input variables independently. The measurement is based on the difference between the minimum and maximum output values calculated by varying one input parameter while others hold constant values. Therefore, its variation can be affected by the constant value of the inputs that are held fixed, but it can provide a better understanding of the variables in the metamodel that have more influence on the outputs of interest. The sensitivities were computed in the chart of Figure 44 used 1.255 mm as the constant thickness of the fixed input variables.
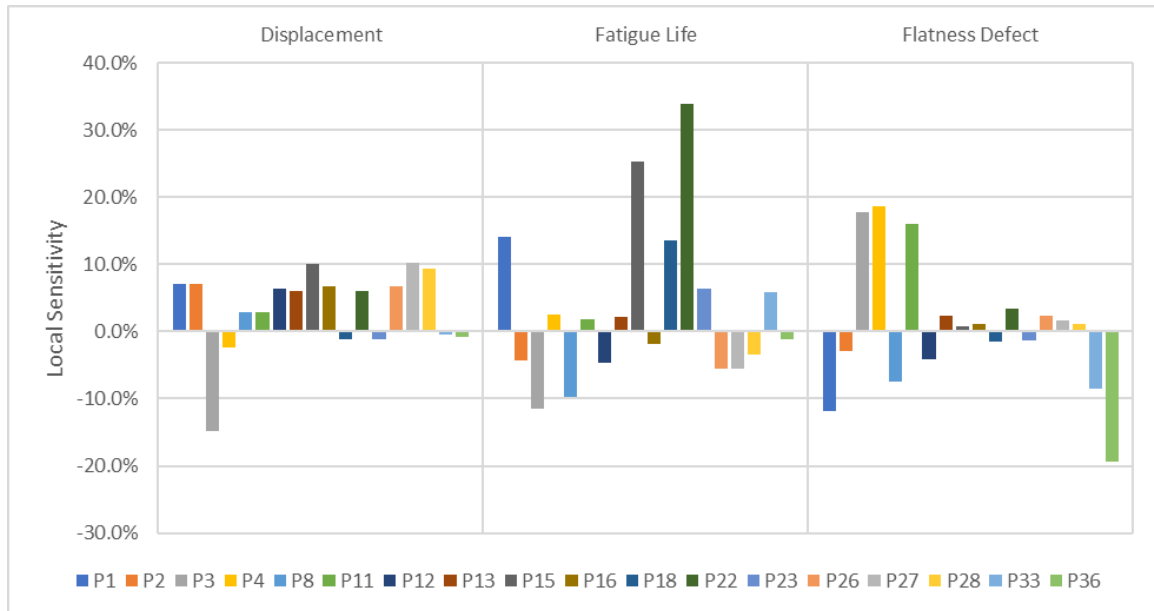
Figure 44 - RSM - Local Sensitivity - Outputs of interest vs Independent Variables

Based on the tolerances set for the case study and on the parameters of quality computed, the response surface generated has a satisfactory predictive performance to be used in the optimization analysis.

5.6.   Optimization

The optimization was implemented to determine the Pareto Front for the three outputs of interest. The convergence is reached when either Pareto percentage or Stability percentage reaches the maximum and minimum set values, respectively. For the case study, the convergence was reached after 34738 evaluations and seven iterations when the calculated stability percentage reached 1.8%, which is lower than the set convergence stability criteria (2%). The calculated Pareto percentage (second optimization convergence criteria) reached 11.89% in eighth iterations that are lower than the maximum set Pareto percentage (70%). For the proposed case study, both convergence thresholds were

arbitrarily defined. Figure 45 depicts the thresholds and calculated values for both Pareto and Stability percentages.
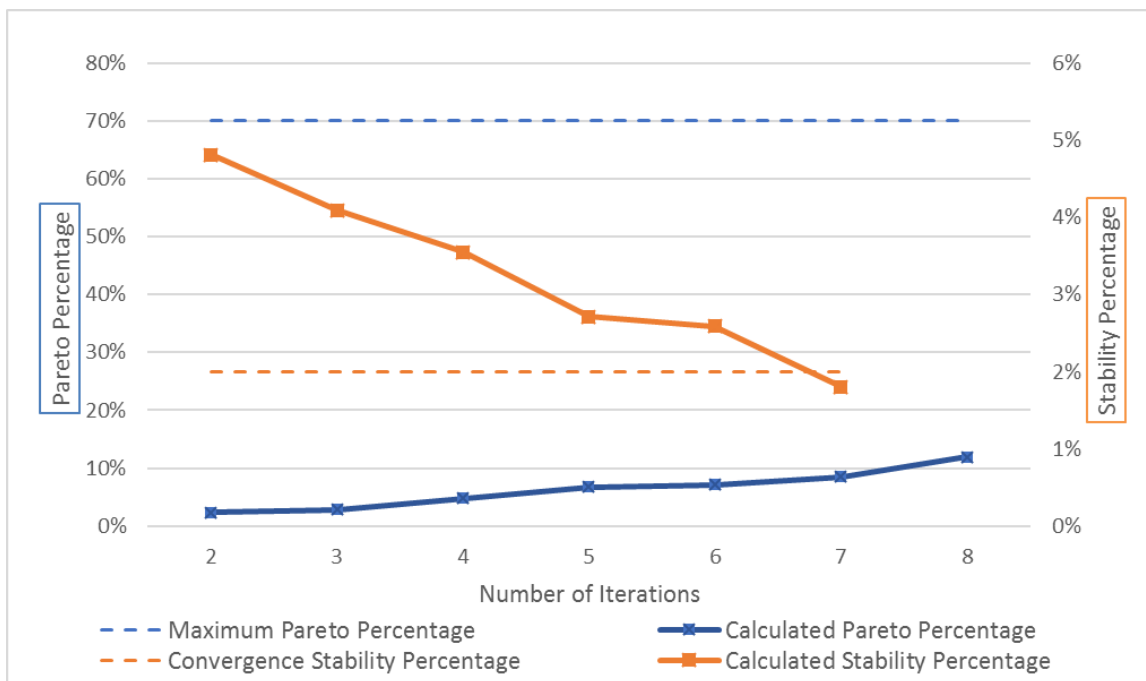
Figure 45 - Optimization convergence criteria – Pareto and Stability percentage

The Pareto front of the three outputs of interest contains the best feasible points derived from the optimization. The 3D trade-off chart in Figure 46 is broken down into three 2D graphs (Figures 46 to 49) to allow better visualization of the distribution of the viable points.
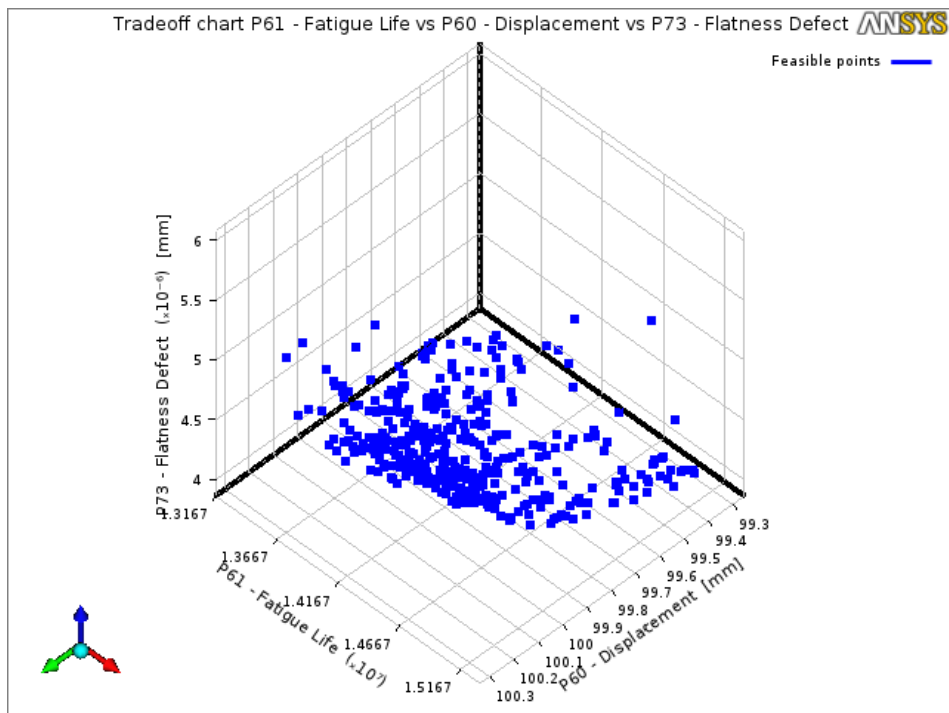
Figure 46 – Tradeoff Chart: 3D Pareto-front [19]
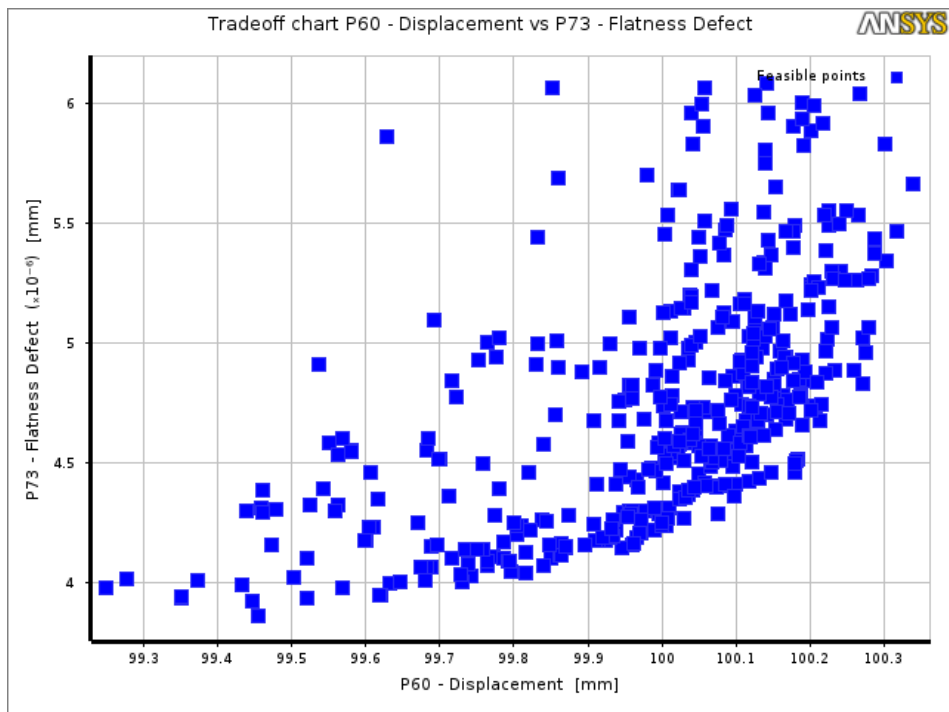
Figure 47 - Pareto Front Projection: Displacement vs Flatness Defect [19]
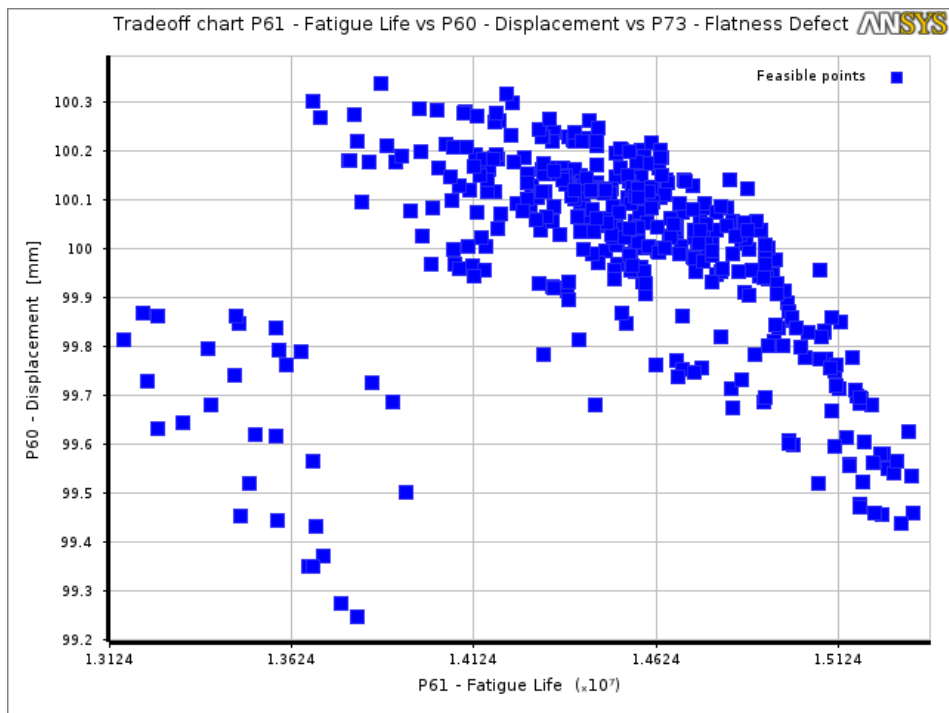
Figure 48 - Pareto Front Projection: Fatigue Life vs Displacement [19]
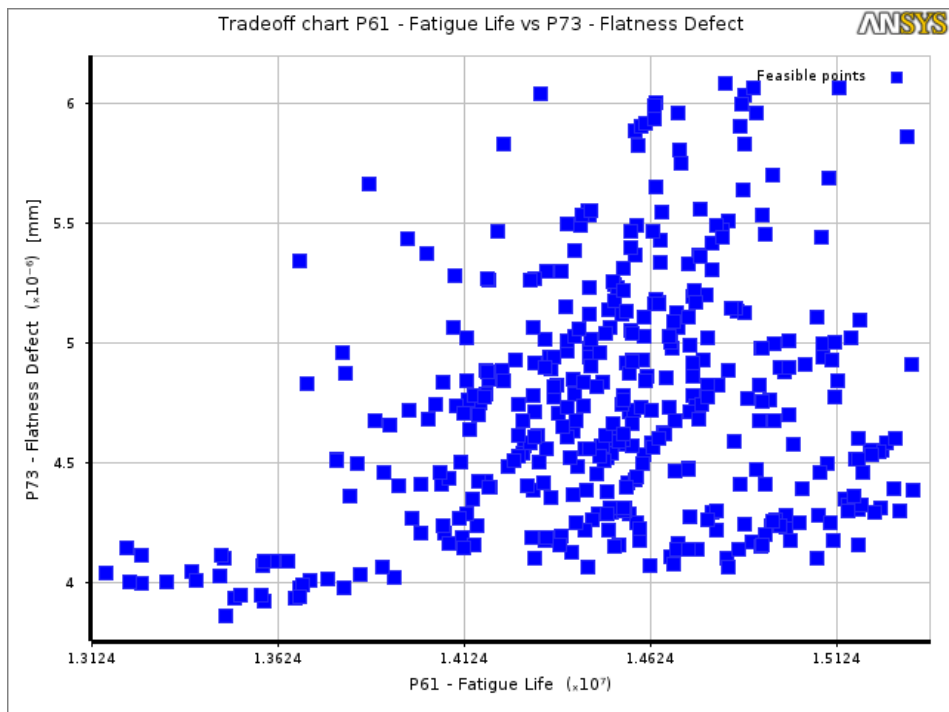
Figure 49 - Pareto Front Projection: Fatigue Life vs Flatness Defect [19]

The output global sensitivities chart shown in Figure 50, demonstrates how the outputs are sensitive to each input variable while interacting with the others. Differently from Local sensitivities, Global sensitivities are computed based on the correlation of all generated sample points and hence do not depend on the values held by the input parameters.
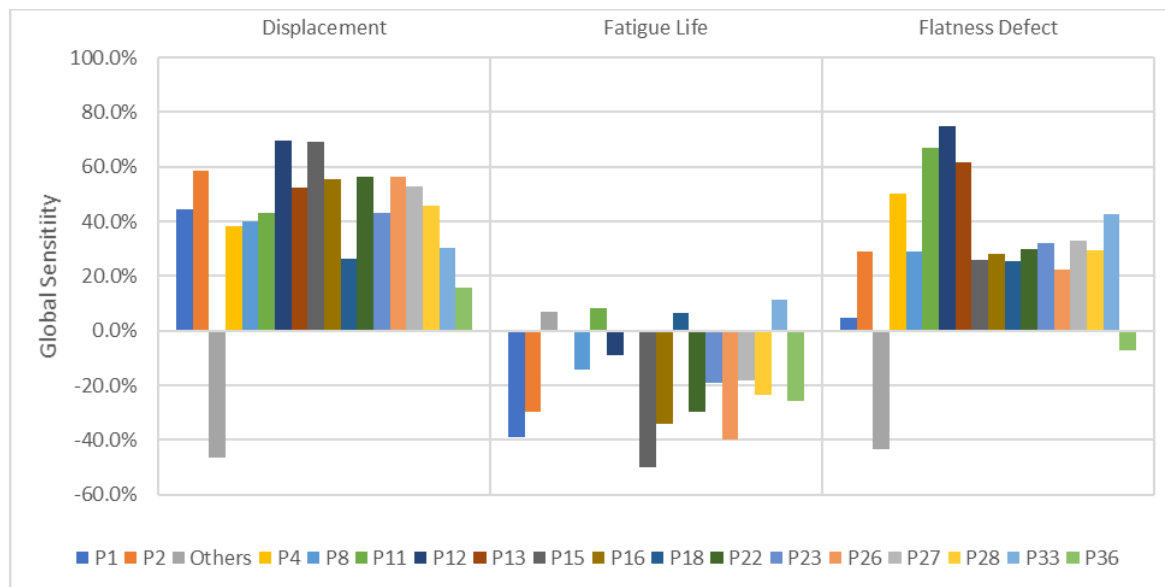
Figure 50 - Outputs Global Sensitivities based on the Optimization analysis

The candidate points, selected from the Pareto-Front, were calculated based on the decision support process, which is a goal-based, weighted, aggregation-based design ranking method, that takes into consideration the importance level of objectives and constraints and the feasibility of the points [28].

The results of the three candidate points are plotted in green in the normalized chart of Figure 52, among other Pareto Front outputs plotted in red.
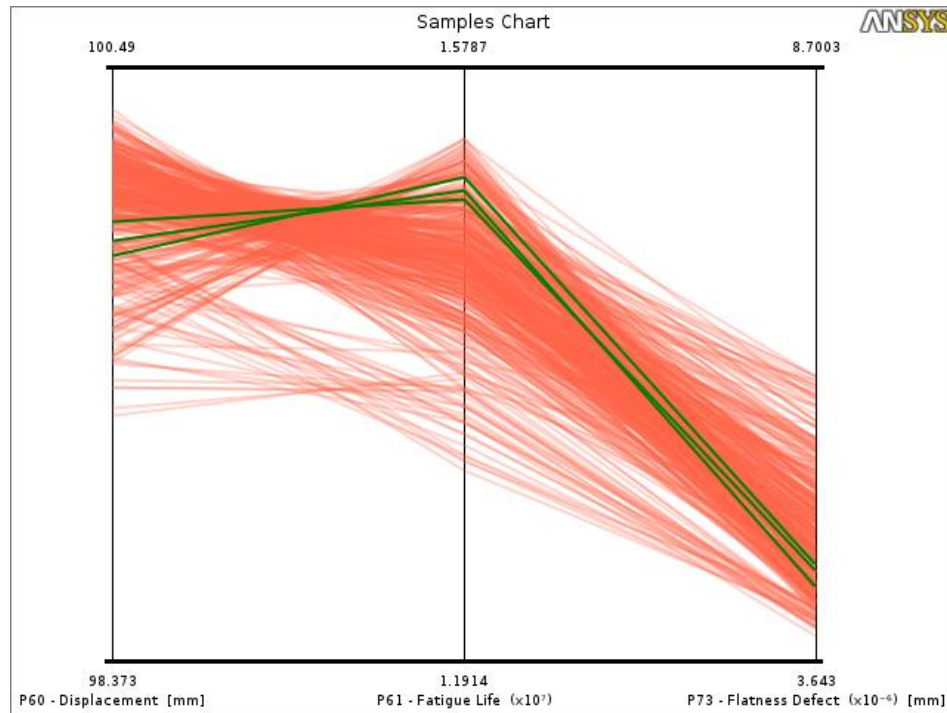
Figure 51 - Optimization – Pareto-Front and Candidate points [19]

The non-dominated samples were ranked to form the Pareto Front to determine the best candidate points based on the values calculated in Equation 22.

5.7. Optimized Results

The values of the three best-rated candidate points are presented in Table 21.

Table 21 – Candidate Points computed from the RSM – Best-Case

	Candidate 1	Candidate 2	Candidate 3
Fatigue Life [cycles]	1.508E7	1.493E7	1.499E7
Displacement [mm]	99.822	99.939	99.874
Flatness Defect [mm]	4.464	4.415	4.283

The Pareto optimal assembly input parameters were analyzed with the nonlinear FE model, and the verified outputs are presented in Table 22. Candidate 1 was chosen as the optimum solution due to the best rating value on the fatigue life parameter among the three candidate points.

Table 22 – Candidate Points verified by the FE predictive model – Best-Case

	Candidate 1	Candidate 2	Candidate 3
Fatigue Life [cycles]	1.509E7	1.471E7	1.466E7
Displacement [mm]	99.798	99.970	99.922
Flatness Defect [mm]	4.164	4.403	4.253

The optimal solution computed from the RSM, the values derived from the FEA verification simulation and respective rating scores (Equation 23) are listed in Table 23. The optimum outputs are compared to the ideal and non-ideal shimless conditions.

Table 23 - Outputs Summary – Non-Ideal Parts Assembly – Best-Case

Assembly Type	Displacement [mm]	Flatness Defect [mm]	Max Von Mises Stress [MPa]	Fatigue Life [cycles]
Ideal Parts	100.65	0.625	203.8	1.365 E7
Non-ideal Parts – No shims	98.992	3.123	204.08	1.343 E7
Non-ideal Parts – Best Case - RSM	99.822	4.464	-	1.508 E7
Non-ideal Parts – Best Case – FEA Verification	99.798	4.164	202.03	1.509 E7
Rating	-1	-2		-2

The 36 shims thickness distribution for the best-case condition are listed in Table 24 and illustrated in Figure 52.

Table 24 - Calculated Shims Thickness distribution – Best-case Results

P1	P2	P3	P4	P5	P6
2.178521	2.150554	0.598995	0.097213	0.598995	0.598995
P7	**P8**	**P9**	**P10**	**P11**	**P12**
0.598995	1.444126	0.598995	0.598995	0.613737	0.999998
P13	**P14**	**P15**	**P16**	**P17**	**P18**
0.17177	0.598995	1.242087	1.085075	0.598995	1.946935
P19	**P20**	**P21**	**P22**	**P23**	**P24**
0.598995	0.598995	0.598995	1.268786	1.548653	0.598995
P25	**P26**	**P27**	**P28**	**P29**	**P30**
0.598995	1.391633	2.480432	2.134518	0.598995	0.598995
P31	**P32**	**P33**	**P34**	**P35**	**P36**
0.598995	0.598995	1.879557	0.598995	0.598995	0.922373
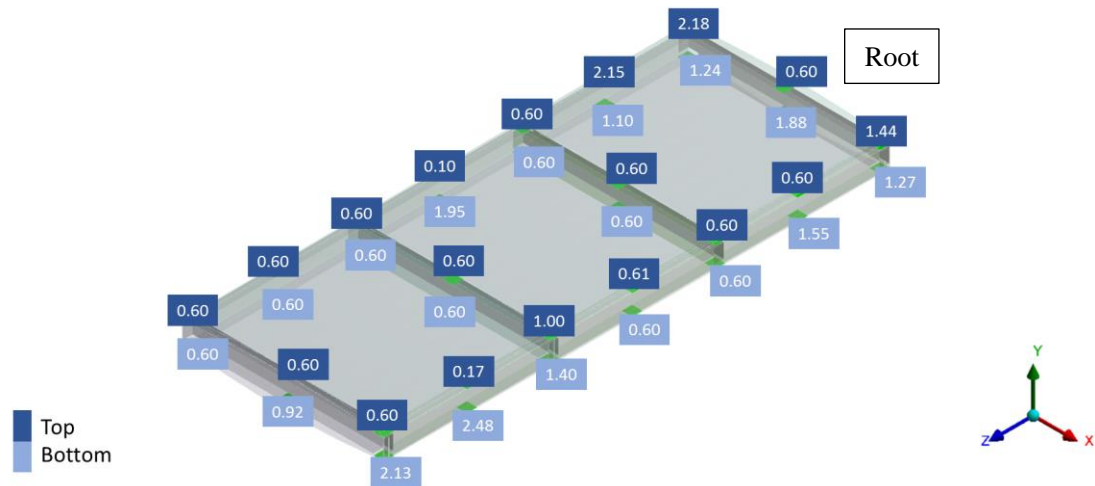
Figure 52 - Shimming Map with Rounded thicknesses - Best-Case [19]

The plots of the optimal outputs are shown in Figures 53 to 57. The Box Tip, under the influence of the 3000N force, displaced 0.852 mm less in the Y direction compared to the assembly with ideal parts.
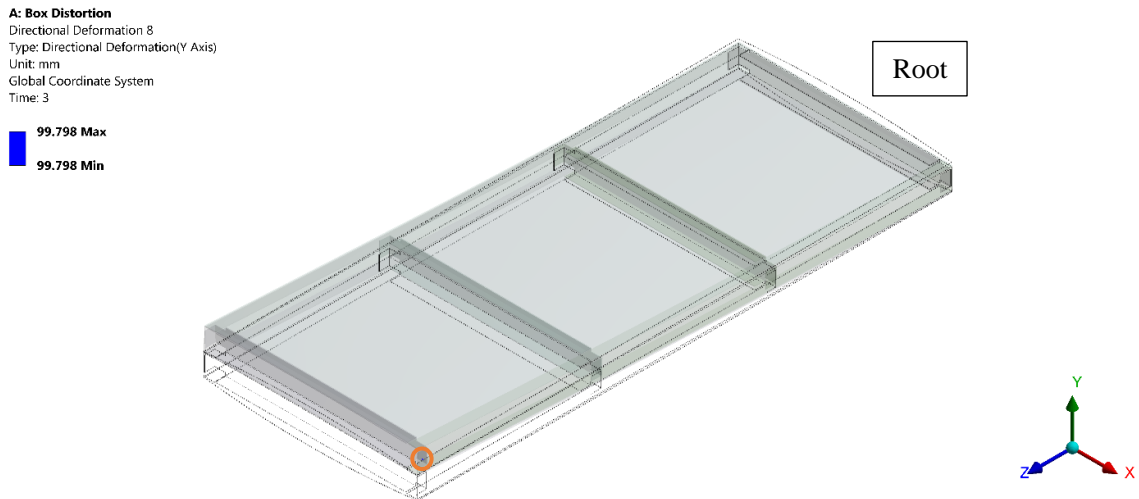
Figure 53 – Non-ideal (shimmed) - Box Tip Displacement at Step 3 - Best Case [19]

The upper skin, shown in Figure 54, develops an asymmetric flatness defect with 4.164 mm maximum amplitude in the Y direction.
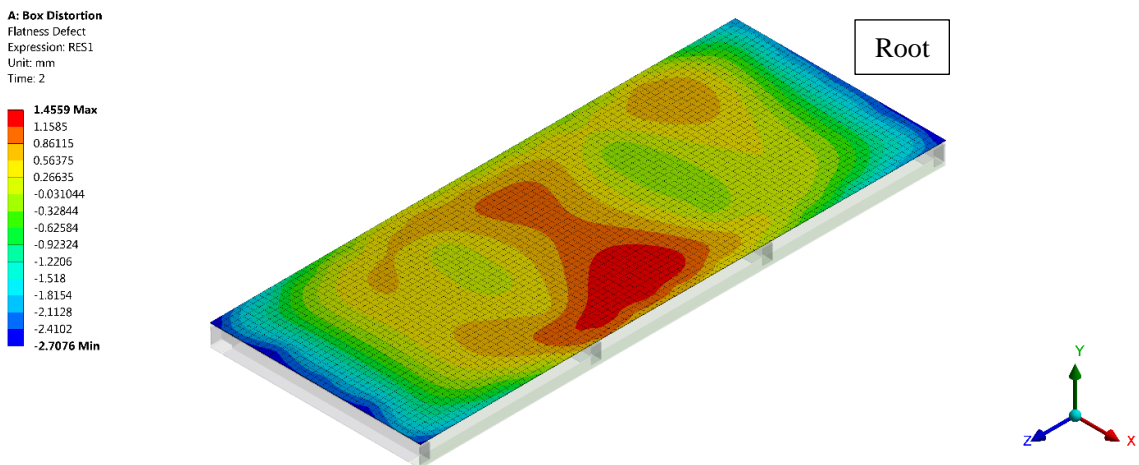
Figure 54 – Non-ideal (shimmed) - Upper Skin Total Flatness Defect in Step 2 – Best-case [19]

Figures 55 to 57 show the stress distribution in the entire structure and spars, respectively. The higher stress distributions were found in the spar's flanges at the root area.
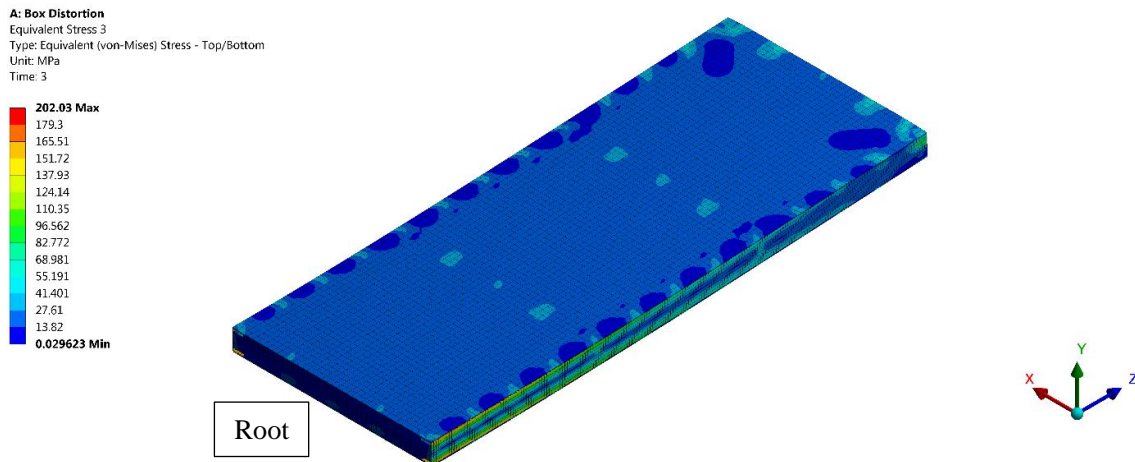
Figure 55 - Non-ideal (shimmed) - Box von Mises Stress in Step 3 – Best-case [19]
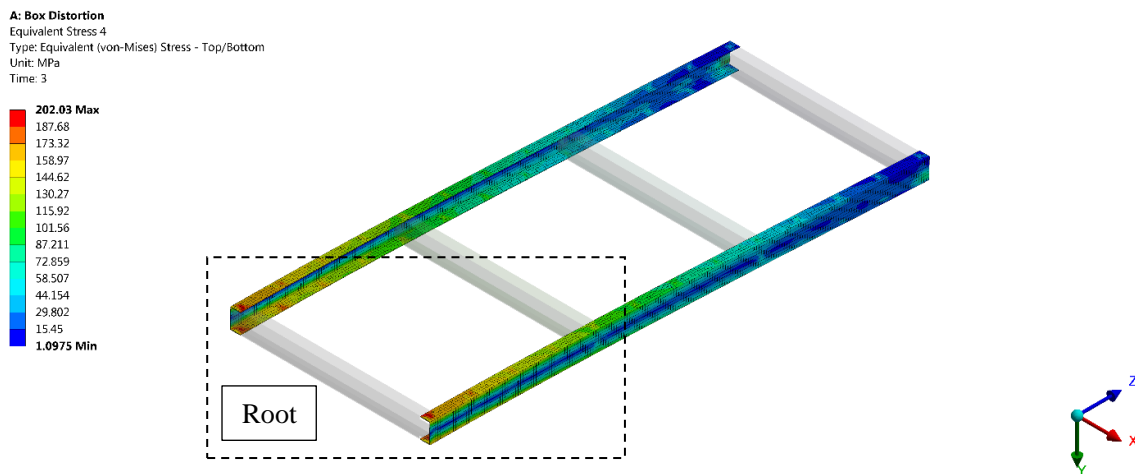
Figure 56 - Non-ideal (shimmed) - Spars von Mises Stress in Step 3 – Best-case [19]
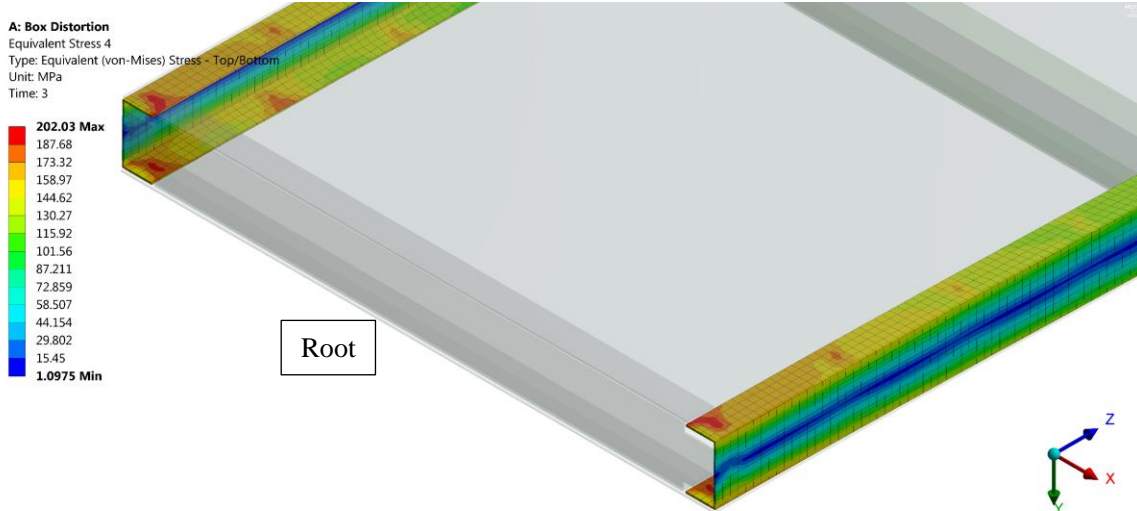
Figure 57 - Non-ideal (shimmed) - Spars von Mises Stress in Step 3 – Best-case – Detail [19]

The fatigue life was measured along the spars, and the lowest number of cycles occur in the flanges at the root area as expected, as presented in Figure 58.
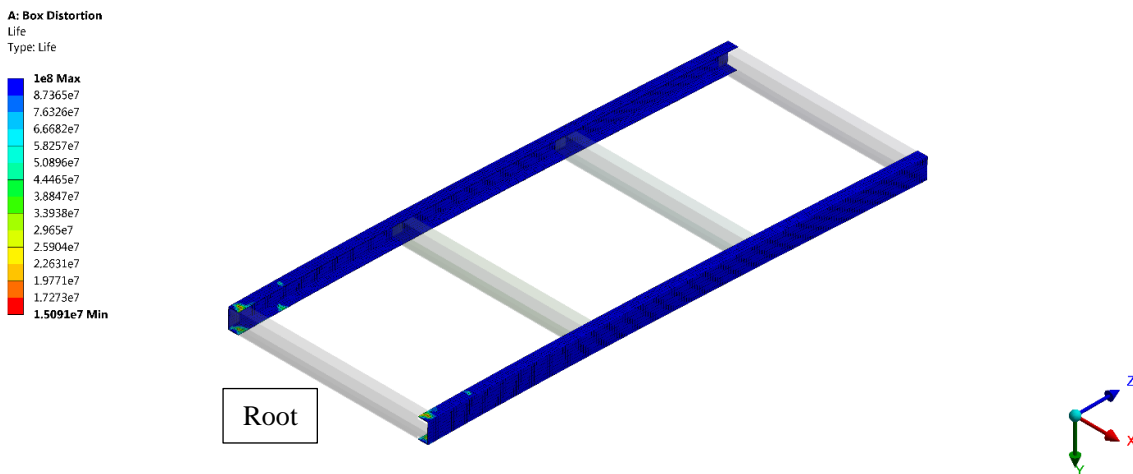
Figure 58 – Non-ideal (shimmed) - Spars Fatigue Life at 0-3000N cyclical load – Best-case [19]

5.8.   Worst Case Results

An optimization analysis was performed to determine the worst-case outputs and provide an understanding of the range of distortions of the assembled structure caused by different shimming strategies. The objective problem is the inverse of the one set for searching the best-case assembly condition but set to be maximized, as presented in Equation 25.

$$\max \begin{cases} \Delta\delta = |a - F(X)| \\ -n = G(X) \\ f_{max} = H(X) \end{cases} \tag{25}$$

$$s.t. \{0.01 \leq X \leq 2.5mm$$

where $\Delta\delta$ is the difference between the displacements of the loaded tip box ideal assembly a (with ideal parts) and the assembly simulated F; n is the maximum number of cycles under a zero-based stress life analysis with no mean stress correction theory considered; f_{max} is the maximum flatness defect measured on the upper skin before the box is released to spring back and subjected to the loading and gravity, and X is the shims thickness vector.

In Table 25, the RSM and FEA-verified worst-case outputs selected from the computed candidate points are presented and compared to the ideal, non-ideal shimless and best-case conditions.

Table 25 - Outputs Summary – Non-Ideal Parts Assembly - Worst-case

Assembly Type	Displacement [mm]	Flatness Defect [mm]	Max Von Mises Stress [MPa]	Fatigue Life [cycles]
Ideal Parts	100.65	0.625	203.8	1.365 E7
Non-ideal Parts – No shims	98.992	3.123	204.08	1.343 E7
Non-ideal Parts – Best Case	99.798	4.164	202.03	1.509 E7
Non-ideal Parts – Worst Case - RSM	98.676	7.060	-	1.319 E7
Non-ideal Parts – Worst Case FEA Verification	98.564	7.150	204.89	1.283 E7
Rating	+3	-2		-2

The 36 shims thicknesses for the worst-case condition are listed in Table 26.

Table 26 - Calculated Shims Thickness distribution – Worst-case Results

P1	P2	P3	P4	P5	P6
0.061635	0.075287	2.440568	2.415982	2.440568	2.440568
P7	**P8**	**P9**	**P10**	**P11**	**P12**
2.440568	0.228412	2.440568	2.440568	2.037779	0.050916
P13	**P14**	**P15**	**P16**	**P17**	**P18**
0.461727	2.440568	0.217776	0.247883	2.440568	0.241375
P19	**P20**	**P21**	**P22**	**P23**	**P24**
2.440568	2.440568	2.440568	0.373624	0.242002	2.440568
P25	**P26**	**P27**	**P28**	**P29**	**P30**
2.440568	0.481949	0.022968	0.051231	2.440568	2.440568
P31	**P32**	**P33**	**P34**	**P35**	**P36**
2.440568	2.440568	0.016977	2.440568	2.440568	0.180314

The plots of the worst-case outputs are illustrated in Figures 59 to 64.

A: Box Distortion
Directional Deformation 8
Type: Directional Deformation(Y Axis)
Unit: mm
Global Coordinate System
Time: 3

98.564 Max
98.564 Min

Root
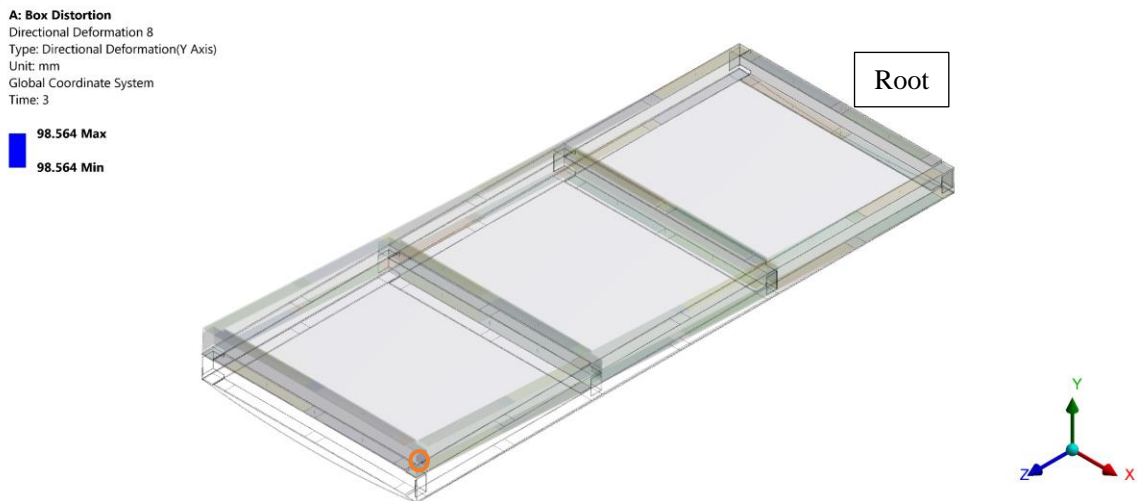
Figure 59 – Non-Ideal (shimmed) - Box tip displacement in Step 3 – Worst-case [19]

A: Box Distortion
Flatness Defect
Expression: RES1
Unit: mm
Time: 2

2.1798 Max
1.6691
1.1584
0.64773
0.13703
-0.37367
-0.88437
-1.3951
-1.9058
-2.4165
-2.9272
-3.4379
-3.9486
-4.4593
-4.97 Min

Root
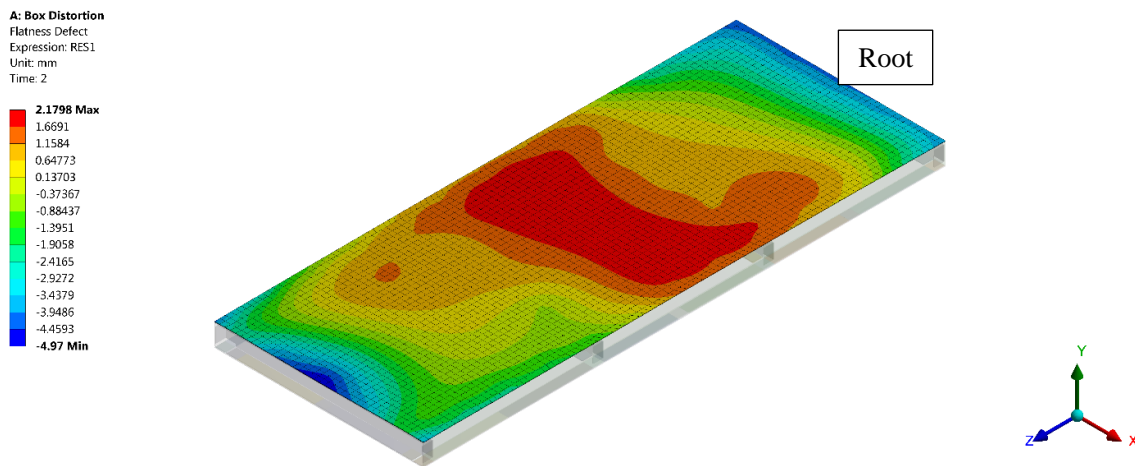
Figure 60 – Non-Ideal (shimmed) - Upper Skin Flatness Defect in Step 2 – Worst-case [19]

Figure 61 – Non-Ideal - Box von Mises Stresses in Step 3 – Worst-case [19]
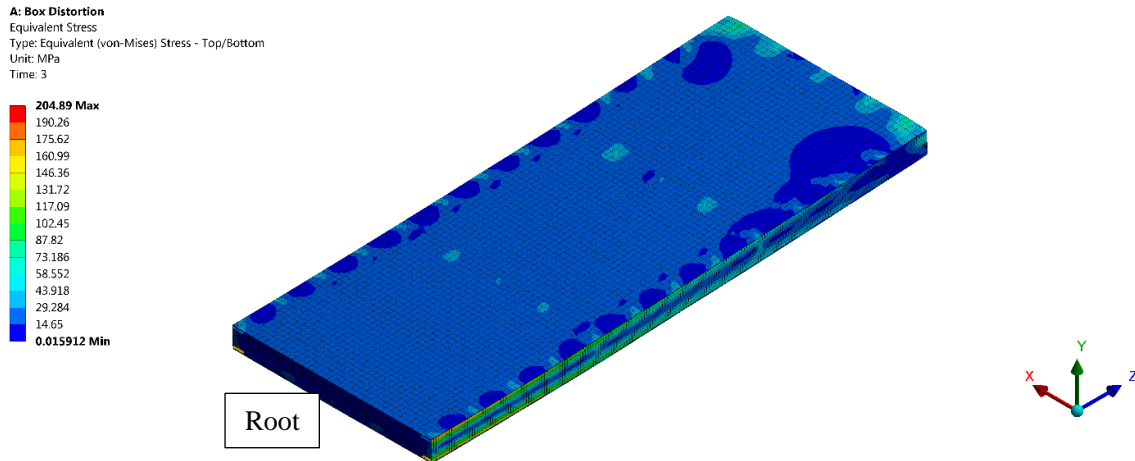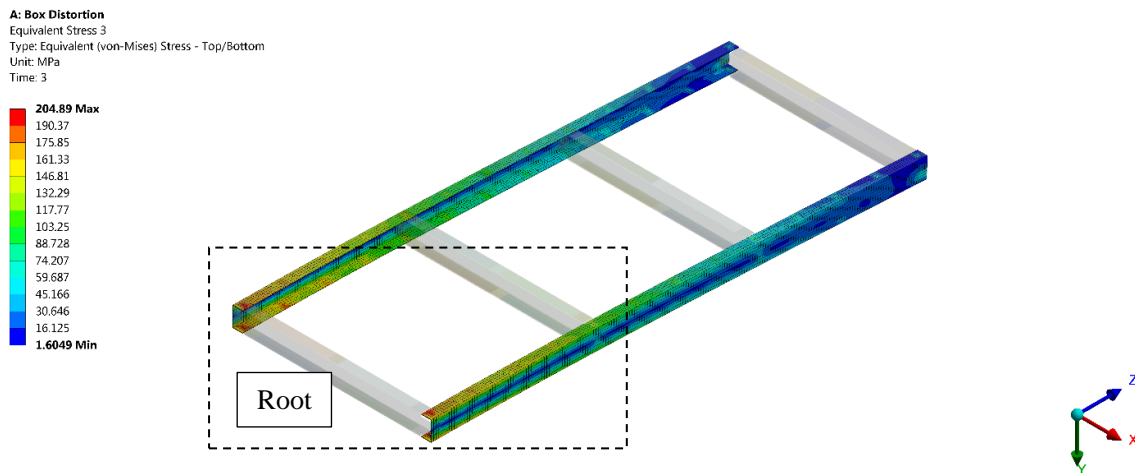

Figure 62 – Non-Ideal (shimmed) - Spars von Mises Stresses in Step 3 – Worst-case [19]
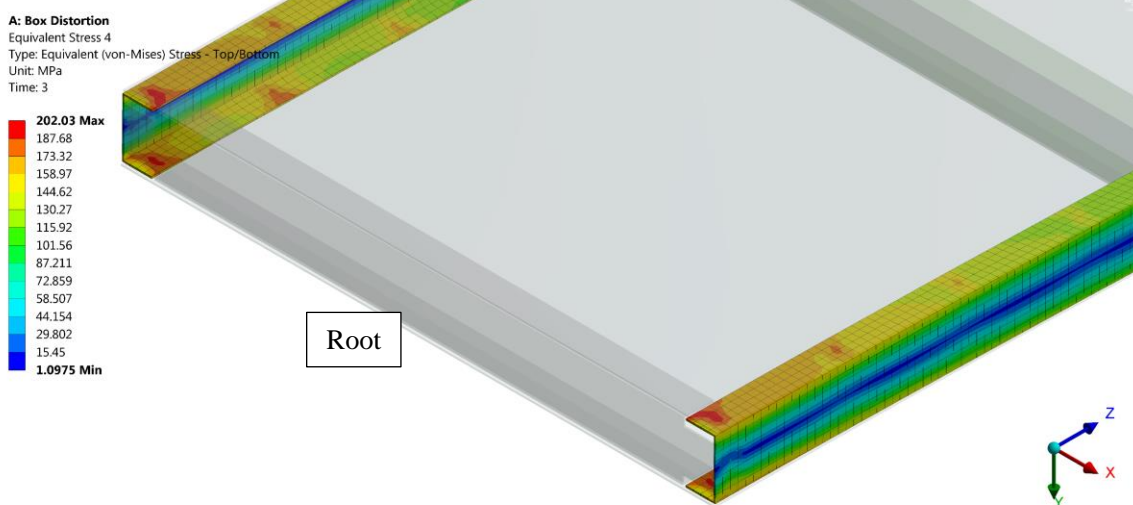
Figure 63 - Non-Ideal (shimmed) - Spars von Mises Stresses in Step 3 – Worst-case – Detail [19]
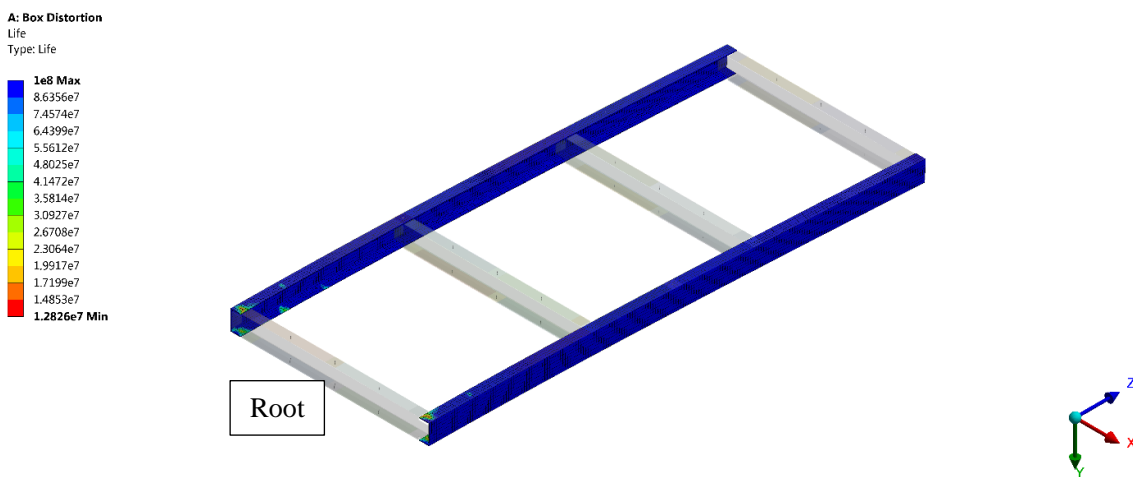
Figure 64 – Non-Ideal (shimmed) - Spars Fatigue at 0-3000N cyclical load – Worst-case [19]

6 - Conclusions

In this work, a state-of-the-art methodology to predict and mitigate excessive distortions and residual stresses in complied assembled structures is presented. In this section, the considerations about the methodology, the results of the case study, the suggestions for future developments and the final considerations are outlined in the following sub-sections.

6.1. Methodology Analysis

The developed methodology was applied in an arbitrary assembled structure, and its accuracy and response time were assessed and verified. Some of the main development challenges described in Section 3.1 were addressed by the modelling and statistical analysis approaches, as summarized in Table 27.

Table 27 - Development challenges and Approach

Challenge	Approach
Accuracy of the scanned geometries	Inverse Solving Analysis (ISA)
Accuracy of the predictive model	Nonlinear Analysis – Contact and Large Displacements
Locking problems in bending loads	Shell Elements
High number of degrees of freedom	
Design space dimension	Correlation Analysis
Computational cost and time consuming	Response Surface Modeling
Multi-Objective optimization problems	Multi-Objective Genetic Algorithm

A procedure based on ISA [21] was used to pre-process the scanned geometries. The gravity and constraining forces were omitted from the virtually deformed upper skin by the proposed method. In simulation conditions, the inverse solving analysis demonstrated good accuracy to prepare scanned data into raw geometries that can be used as a reference in the predictive model.

A methodology to create the predictive model, considering large displacements and contact, was developed based on nonlinear FEA. The model was implemented using shell elements to balance output accuracy and processing time and to prevent shear locking issues under bending loads.

A correlation analysis was performed to reduce the problem dimension from 36 to 17 parameters based on the coefficients of correlation r and determination R^2. With the most critical input variables defined, the metamodel was developed based on the Genetic Aggregation Response Surface algorithm [19], which is an ensemble of Full 2nd-Order Polynomials and Kriging methods as detailed in Table 19. As observed in the Predicted vs Observed charts (Figure 38 - 40) and in the goodness of fit quality parameters in Table 20, the metamodel presents a precise approximation over the learning points but some losses in the cross-validation analysis. Based on the relative low errors found in the verification points and the deviation in the MRR and RMAE parameters from the cross-validation analysis, it is likely that these losses resulted from the high dependence of the metamodel to the design points sampled rather than overfitting and bias. Thus, the derived metamodel was considered satisfactory as a computational source for the optimization analysis.

MOGA was applied in the metamodel to determine the first Pareto Front and identify the most significant feasible points for the best and worst-case assembly conditions of the case study. The best three candidate points were selected from the Pareto Front based on the rating computed by the decision support process. The candidate points were verified through the FE predictive model, and the output errors between the metamodel and the FE model were calculated, as presented in Table 28. The low absolute errors of the metamodel

indicate a satisfactory performance of the methodology to predict the process, enabling the search of optimum solutions in the design space within a reasonable time frame.

Table 28 - Candidate Points Absolute Errors - Best-Case - Metamodel vs FEA

	Candidate 1	**Candidate 2**	**Candidate 3**
Fatigue Life	0.07%	1.51%	2.24%
Displacement	0.02%	0.03%	0.05%
Flatness Defect	7.21%	0.26%	0.71%

6.2.   Case Study Results Analysis

The ISA method, used to omit the deformations caused by the gravity and clamping effects on the scanned geometry, was tested under simulation conditions. The 0.05 mm tolerance reached by the recovered geometry in comparison to the original upper skin is satisfactory for the proposed application, which validates the proposed method.

The shim thickness distribution of the best and worst-case, derived from the metamodel, was verified using the FEA model and compared to the ideal and the non-ideal shimless assembly conditions, as summarized in Table 29.

Table 29 - Outputs for different assembly conditions

Assembly Type	Displacement [mm]	Flatness Defect [mm]	Max von Mises Stress [MPa]	Fatigue Life [cycles]
Ideal Parts	**100.65**	**0.625**	**203.8**	**1.365 E7**
Non-ideal Parts – No shims	98.992	3.123	204.08	1.343 E7
Non-ideal Parts – Best Case FEA	99.798	4.164	202.03	1.509 E7
Non-ideal Parts – Worst Case FEA	98.564	7.150	204.89	1.283 E7

Based on the results computed in the case study under different assembly conditions, the following outcomes are outlined:

1. Optimized shimming strategies have the potential to improve the fatigue performance of compliant assembled structures composed of non-ideal parts. In the case study, the fatigue life of the assembled box was improved by 10.5% when compared to the ideal configuration, which was derived from the initial distortion of the spars that lead to a 0.87% reduction in von Mises stresses at the spars root areas for the applied loading condition.

2. The deflections caused by the loading conditions in the assembled structure are affected by its stiffness, the shim thickness range and the induced moment of the compliant forces. In the case study, the 1.234 mm tip displacement variation between the best- and worst-case shimming configurations were obtained using 0.1-to-2.5 mm shim thickness range in a 2.5 x 1.0 x 0.1 m structure length. Thus, it is expected that longer and slender structures present a wider displacement variation caused by the differences in shimming strategies, that might also be increased by using thicker shims.

3. The total flatness defect is highly affected by the distorted parts and the selected shimming strategy. For the shimless assembly strategy, the flatness defect increased by approximately 400% compared to the assembly composed of ideal parts. Considering that the minimization of the flatness defect was set with lower importance in the optimization, the selected best solution increased the flatness defect by 33%, i.e. from 3.123 mm in the shimless condition to 4.164 mm.

4. It is observed in the case study that an improper assembly strategy can degrade all the outputs substantially, as presented in the worst-case assembly condition. Under such circumstances, the fatigue performance declined by 15% compared to the best

shimming strategy, the delta displacement increased by 2.086 mm downwards compared to the ideal-parts assembly, and the flatness defect increased more than ten times the ideal condition.

5. In case a small loss in fatigue life is acceptable, a shimless strategy could be considered an interesting alternative due to its reduced production cost, as shims fabrication and installation would not be required. In the case study, though the shimless assembly degraded the fatigue life by 1.6% in comparison to the ideal-parts condition, the structure presented a better performance in delta displacement (1.658 mm) and total flatness defect (3.123 mm) compared to others shimmed assembly conditions analyzed.

6. Processing time is a relevant parameter in decision tools applied to production processes. The elapsed time of the main analysis steps applied in the case study is presented in Table 30. The results were computed based on an Intel i7-3720QM 2.60 GHz – 16GB RAM – NVIDIA Quadro 1000M graphic card hardware.

Table 30 - Computational Time of the main analysis steps

	Iterations	Elapsed Time
Simulation Run (Non-ideal assembly model)	1	0.2 hours
Correlation Analysis	185	34 hours
DOE – Response Surface	255	47 hours
Optimization	45358	5 hours

As observed in Table 21, the correlation analysis and the response surface modelling are the more time-consuming steps in the methodology. The longer elapsed time is caused by the computational demand of the nonlinear FEA model,

which takes about 0.2 hours per run. Conversely, the metamodel used in the optimization step takes about 0.4 seconds to complete each run. However, even with a limited hardware, the methodology provided the assembly strategy response in 3.6 days for the case study. In general, the lead time between the end of the inspection and the end of the pre-assembly process for medium to large aerostructures demand several days or weeks due to the complementary processes and logistics lead times. Thus, the analysis response of the proposed case study, computed in limited hardware, indicates a tendency of the methodology to not create negative impacts on the production schedule.

6.3.   Future Developments

Some critical aspects of the analysis were not considered in this study, due to the limitation of resources and/or the necessity of keeping the scope of the work bounded. The following observations are suggestions that can potentially benefit the quality and performance of the analysis and should be considered in future studies related to the topic of this work.

There exists an opportunity, in terms of processing time, for future developments through the use of high-performance computing (HPC) cloud environments. The use of more efficient processing hardware might enable the introduction of additional process variables and complexity without compromising the time frame available in the production line.

Distortions and stresses in the holes caused by the installation of fasteners were not considered in this study. The influence of such stresses on the overall distortion of assembled structures is a relevant issue to be evaluated, as presented by Liu et al. [38] and Figueira et al. [39]. Therefore, it would be beneficial to evaluate modelling strategies that

allow the inclusion of the fasteners' effects in the model with a low impact on its processing performance.

ISA method was used to omit the effects of boundary conditions and loadings under the simulation environment. In order to allow a proper validation of the method and to implement eventual adjustments, it would be essential to evaluate how the noises of the scanning processes could affect the analysis and the accuracy of the recovered geometry.

Although the methodology was developed in Ansys [19, 21], which is a mature FEA platform, the results of the case study were not validated with physical experiments. The use of real-world structures in a case study would allow further adjustments on the methodology and consequently improve the accuracy of the responses and decisions made in the assembly line.

6.4.   Final Considerations

In conclusion, the present methodology and case study results demonstrated the viability of applying nonlinear FE models and optimization procedures to determine optimum assembly strategies within a reasonable time frame for industrial applications. The outputs computed in this study indicate that proper shimming strategies could potentially mitigate or reverse adverse effects in product performance caused by distorted components, whereas incorrect shimming schemes might further degrade all quality parameters of the structure. In fact, the proposed methodology creates conditions for a thorough quantitative evaluation of several alternative assembly configurations that would not be possible without proper integration of the capabilities of nonlinear FEM, statistical analysis, meta modelling and optimization techniques.

7 - Bibliography

[1] Saadat, M., 2011. Challenges in the Assembly of Large Aerospace Components, in: Fathi, M., Holland, A., Ansari, F., Weber, C. (Eds.), Integrated Systems, Design and Technology 2010. Springer, Berlin, Heidelberg, pp. 37–46. https://doi.org/10.1007/978-3-642-17384-4_4

[2] Withers, P.J., Bhadeshia, H.K.D.H., 2001. Residual stress. Part 2 – Nature and origins. Materials Science and Technology 17, 366–375. https://doi.org/10.1179/026708301101510087

[3] Liu, S.C., Hu, S.J., 1997. "Variation Simulation for Deformable Sheet Metal Assemblies Using Finite Element Methods." J. Manuf. Sci. Eng 119, 368–374. https://doi.org/10.1115/1.2831115

[4] Swartz, K.I., n.d. Wings to fly. Skies Mag. URL https://www.skiesmag.com/features/wings-to-fly/ (accessed 3.11.20).

[5] Using Laminated Shims [WWW Document], n.d. URL https://www.assemblymag.com/articles/93341-using-laminated-shims?v=preview (accessed 5.15.20).

[6] Camelio, J., Hu, S.J., Ceglarek, D., 2003. Modeling variation propagation of multi-station assembly systems with compliant parts. J. Mech. Des. 125, 673–681.

[7] Camelio, J.A., Hu, S.J., Marin, S.P., 2004. "Compliant Assembly Variation Analysis Using Component Geometric Covariance. Journal of Manufacturing Science and Engineering" 126, 355. https://doi.org/10.1115/1.1644553

[8] Dahlström, S., Lindkvist, L., 2006. Variation Simulation of Sheet Metal Assemblies Using the Method of Influence Coefficients With Contact Modeling. Journal of Manufacturing Science and Engineering 129, 615–622. https://doi.org/10.1115/1.2714570

[9] Ungemach, G., Mantwill, F., 2008. Efficient Consideration of Contact in Compliant Assembly Variation Analysis. Journal of Manufacturing Science and Engineering 131, 011005-011005–9. https://doi.org/10.1115/1.3046133

[10] Xie, K., Wells, L., Camelio, J.A., Youn, B.D., 2007. "Variation Propagation Analysis on Compliant Assemblies Considering Contact Interaction." J. Manuf. Sci. Eng 129, 934–942. https://doi.org/10.1115/1.2752829

[11] Liao, X., Wang, G.G., 2007. Nonlinear dimensional variation analysis for sheet metal assemblies by contact modelling. Finite Elements in Analysis and Design 44, 34–44. https://doi.org/10.1016/j.finel.2007.08.009

[12] Wriggers, P., 2008. Nonlinear Phenomena, in: Wriggers, P. (Ed.), Nonlinear Finite Element Methods. Springer Berlin Heidelberg, Berlin, Heidelberg, pp. 7–18. https://doi.org/10.1007/978-3-540-71001-1_2

[13] Li, Y., Zhao, Y., Yu, H., Lai, X., 2019. Modelling deviation propagation of compliant assembly considering form defects based on basic deviation fields. Assembly Automation.

[14] Yue, J., Camelio, J.A., Chin, M., Cai, W., 2007. Product-Oriented Sensitivity Analysis for Multistation Compliant Assemblies. J. Mech. Des 129, 844–851. https://doi.org/10.1115/1.2735341

[15] Dong, C., Kang, L., 2012. Deformation and stress of a composite–metal assembly. Int J Adv Manuf Technol 61, 1035–1042. https://doi.org/10.1007/s00170-011-3757-9

[16] Hu, S.J., Camelio, J., 2006. Modelling and Control of Compliant Assembly Systems. CIRP Annals 55, 19–22. https://doi.org/10.1016/S0007-8506(07)60357-6

[17] Wang, H., Ding, X., 2013. Identifying sources of variation in horizontal stabilizer assembly using finite element analysis and principal component analysis. ASSEMBLY AUTOMATION 33, 86–96. https://doi.org/10.1108/01445151311294847

[18] Wang, H., 2015. Highly Efficient Selective Assembly Method of Horizontal Stabilizer based on Metamodelling and Particle Swarm Optimization. JOURNAL OF AEROSPACE ENGINEERING 28. https://doi.org/10.1061/(ASCE)AS.1943-5525.0000424

[19] Ansys® Academic Research, Release 19.1

[20] Ansys® Academic Student 2019 R3, Mechanical Application 2019 R3, Mechanical User's Guide, ANSYS, Inc.

[21] Ansys® Academic Student 2019 R3

[22] Automated Scanning Solution Speeds Aerospace Manufacturing [WWW Document], n.d.. Hexagon Manufacturing Intelligence. URL https://www.hexagonmi.com/solutions/case-studies/aerospace/automated-scanning-solution-speeds-aerospace-manufacturing (accessed 2.29.20).

[23] Keast, J., 2008. Selecting a Reverse Engineering System, in: Raja, V., Fernandes, K.J. (Eds.), Reverse Engineering: An Industrial Perspective, Springer Series in Advanced Manufacturing. Springer London, London, pp. 71–98. https://doi.org/10.1007/978-1-84628-856-2_4

[24] Ansys® Academic Research Mechanical, Release 19.1, Mechanical Application, Release 19.1, Mechanical User's Guide, ANSYS, Inc.

[25] Liao, X., Wang, G.G., 2007. Nonlinear dimensional variation analysis for sheet metal assemblies by contact modelling. Finite Elements in Analysis and Design 44, 34–44. https://doi.org/10.1016/j.finel.2007.08.009

[26] Walczyk, D.F., Raju, V., Miller, R., 2000. Fixtureless assembly of sheet metal parts for the aircraft industry. PROCEEDINGS OF THE INSTITUTION OF MECHANICAL ENGINEERS PART B-JOURNAL OF ENGINEERING MANUFACTURE 214, 173–182.

[27] Zheng, B., Yu, H., Lai, X., 2017. Assembly deformation prediction of riveted panels by using equivalent mechanical model of riveting process. Int J Adv Manuf Technol 92, 1955–1966. https://doi.org/10.1007/s00170-017-0262-9

[28] Ansys® Academic Research, Release 19.1, Workbench, Release 19.1, Workbench User's Guide, ANSYS, Inc.

[29] Yin, H., Fang, H., Wen, G., Gutowski, M., Xiao, Y., 2018. On the ensemble of metamodels with multiple regional optimized weight factors. Struct Multidisc Optim 58, 245–263. https://doi.org/10.1007/s00158-017-1891-1 [21] Ansys® Academic Student 2019 R3, Workbench 2019 R3, Workbench User's Guide, ANSYS, Inc.

[30] Loose, J.-P., Chen, N., Zhou, S., 2009. Surrogate modelling of dimensional variation propagation in multistage assembly processes. IIE Transactions 41, 893–904. https://doi.org/10.1080/07408170902906027

[31] Baş, D., Boyacı, İ.H., 2007. Modelling and optimization I: Usability of response surface methodology. Journal of Food Engineering 78, 836–845. https://doi.org/10.1016/j.jfoodeng.2005.11.024

[32] Myers, R.H., Montgomery, D.C., Anderson-Cook, C.M., 2016. Response Surface Methodology: Process and Product Optimization Using Designed Experiments. John Wiley & Sons, Incorporated, New York, UNITED STATES.

[33] Acar, E., Rais-Rohani, M., 2009. Ensemble of metamodels with optimized weight factors. Struct Multidisc Optim 37, 279–294. https://doi.org/10.1007/s00158-008-0230-y

[34] Acar, E., 2010. Various approaches for constructing an ensemble of metamodels using local measures. Struct Multidisc Optim 42, 879–896. https://doi.org/10.1007/s00158-010-0520-z

[35] Viana, F.A.C., Venter, G., Balabanov, V., 2010. An algorithm for fast optimal Latin hypercube design of experiments. International Journal for Numerical Methods in Engineering 82, 135–156. https://doi.org/10.1002/nme.2750

[36] Viana, F.A.C., 2016. A Tutorial on Latin Hypercube Design of Experiments. Quality and Reliability Engineering International 32, 1975–1985. https://doi.org/10.1002/qre.1924

[37] Kramer, O., 2014. Multiple Objectives, in: Kramer, O. (Ed.), A Brief Introduction to Continuous Evolutionary Optimization, SpringerBriefs in Applied Sciences and Technology. Springer International Publishing, Cham, pp. 55–64. https://doi.org/10.1007/978-3-319-03422-5_6

[38] Liu, G., Huan, H., Ke, Y., 2014. Study on analysis and prediction of riveting assembly variation of aircraft fuselage panel. Int J Adv Manuf Technol 75, 991–1003. https://doi.org/10.1007/s00170-014-6113-z

[39] Figueira, J.A.N., Trabasso, L.G., 2015. Riveting-Induced Deformations on Aircraft Structures. JOURNAL OF AIRCRAFT 52, 2032–2050. https://doi.org/10.2514/1.C033140

[40] Mortensen, A.J., n.d. AN INTEGRATED METHODOLOGY FOR STATISTICAL TOLERANCE ANALYSIS OF FLEXIBLE ASSEMBLIES 192.

[41] Wang, H., Liu, J., 2016. Tolerance Simulation of Thin-walled C-section Composite Beam Assembling with Small Displacement Torsor Model. Procedia CIRP 43, 274–279. https://doi.org/10.1016/j.procir.2016.02.015

[42] Gerbino, S., Franciosa, P., Patalano, S., 2015. Parametric Variational Analysis of Compliant Sheet Metal Assemblies with Shell Elements. Procedia CIRP 33, 339–344. https://doi.org/10.1016/j.procir.2015.06.077

[43] Li, J., Wang, S., 2017. Distortion caused by residual stresses in machining aeronautical aluminum alloy parts: recent advances. The International Journal of Advanced Manufacturing Technology 89, 997–1012. https://doi.org/10.1007/s00170-016-9066-6

[44] Saadat, M., Sim, R., Najafi, F., 2007. Prediction of geometrical variations in Airbus wingbox assembly. ASSEMBLY AUTOMATION 27, 324–332. https://doi.org/10.1108/01445150710827104

[45] Saadat, M., Cretin, L., Sim, R., Najafi, F., 2009. Deformation analysis of large aerospace components during assembly. Int J Adv Manuf Technol 41, 145–155. https://doi.org/10.1007/s00170-008-1464-y

[46] Chang, M., Gossard, D.C., 1997. Modelling the assembly of compliant, non-ideal parts. Computer-Aided Design 29, 701–708. https://doi.org/10.1016/S0010-4485(97)00017-1

[47] Merkley, K., 1998, Tolerance Analysis of Compliant Assemblies, Ph.D. Dissertation, Brigham Young University, Provo, Utah.

[48] Davidson, J.K. (Ed.), 2007. Models for Computer Aided Tolerancing in Design and Manufacturing. Springer Netherlands, Dordrecht. https://doi.org/10.1007/1-4020-5438-6

[49] Page, D., Koschan, A., Abidi, M., 2008. Methodologies and Techniques for Reverse Engineering–The Potential for Automation with 3-D Laser Scanners, in: Raja, V., Fernandes, K.J. (Eds.), Reverse Engineering: An Industrial Perspective, Springer Series in Advanced Manufacturing. Springer, London, pp. 11–32. https://doi.org/10.1007/978-1-84628-856-2_2